Flexoelectricity and Surface Effects on Coupled Electromechanical Responses of Graphene Reinforced Functionally Graded Nanocomposites: A unified size-dependent semi-analytical framework

S. Naskar [a,*,1], K. B. Shingare[b,*], S. Mondal[c,*], T. Mukhopadhyay[d,*]

[a]*Faculty of Engineering and Physical Sciences, University of Southampton, Southampton, UK*
[b]*Department of Aerospace Engineering, Indian Institute of Technology Bombay, Bombay, India*
[c]*Department of Mechanical Engineering, National Institute of Technology Durgapur, Durgapur, India*
[d]*Department of Aerospace Engineering, Indian Institute of Technology Kanpur, Kanpur, India*
[1]*Email Address:* S.Naskar@soton.ac.uk

Abstract

Owing to inhomogeneous strain and high surface-to-volume ratio in nanostructures, it is imperative to account for the flexoelectricity as well as surface effect while analyzing the size-dependent electromechanical responses of nano-scale piezoelectric materials. In this article, a semi-analytical 'single-term extended Kantorovich method (EKM)' and 'Ritz method' based powerful framework is developed for investigating the static and dynamic electromechanical responses of graphene reinforced piezoelectric functionally graded (FG) nanocomposite plates, respectively. The residual surface stresses, elastic and piezoelectric surface modulus, and direct flexoelectric effects are taken into account while developing the unified governing equations and boundary conditions. The modified Halpin Tsai model and rules of mixture are implemented to predict the effective bulk properties. Our results reveal that the static deflection and resonance frequency of the proposed FG nanoplates are significantly influenced due to the consideration of flexoelectricity and surface effects. While such outcomes emphasize the fact that such effects cannot be ignored, these also opens up the notion of on-demand property modulation and active control. The effects are more apparent for nanoplates of lesser thickness, but they diminish as plate thickness increases, leading to the realization and quantification of a size-dependent behavior. Based on the developed unified formulation, a comprehensive numerical investigation is further carried out to characterize the electromechanical responses of nanoplates considering different critical parameters such as plate thicknesses, aspect ratios, flexoelectric coefficients, piezoelectric multiples, distribution, and weight fraction of graphene platelets along with different boundary conditions. With the recent advances in nano-scale manufacturing, the current work will provide the necessary physical insights in modeling size-dependent multifunctional systems for active control of mechanical properties and harvesting electromechanical energy.

Keywords: Flexoelectricity and surface effect; Size-dependence in composite materials; Graphene reinforced functionally graded materials; Extended Kantorovich method; Ritz method; Electromechanical responses.

---

[*] All authors have contributed equally

1. Introduction

In recent decades, structures made of smart materials (piezoelectric) such as beams, wires, plates, membranes and shells have intrigued the researchers' interest in developing the micro-/nano-electromechanical systems (M-/NEMS) for structural control and health monitoring applications such as smart actuators, sensors, capacitor, generator and distributors with capabilities of self-monitoring and -controlling (Beeby et al., 2006; Reddy, 1999; Song et al., 2006; Trindade and Benjeddou, 2009; Wang et al., 2006; Deng et al., 2014; Ghasemi et al., 2018). In 1880, French scientists Jacques and Pierre Curie observed piezoelectricity effects for the first time (Curie and Curie, 1880). Later, Gabriel Lippmann deduced mathematical relations for the converse piezoelectric effect from the fundamental thermodynamic principles (Lippmann, 1881), which was not estimated by Curie brothers. The piezoelectric phenomena are well-known for generating electrical response when subjected to uniform mechanical deformation, known as the direct piezoelectric effect. The reverse is also true when the electrical field is applied, known as the converse piezoelectric effect (electromechanical coupling in non-centrosymmetric crystals). The inversion centre is not present in non-centrosymmetric crystalline materials, which results in the generation of polarization when it is exposed to mechanical load. In elementary structures such as beams, wires, plates, membranes and shells, piezoelectric materials can be employed as a viable option for the application of distributed sensors and actuators due to the presence of unique electro-mechanical couplings as discussed above. For instance, both the static as well as dynamic response of functionally graded (FG) piezoelectric bimorph and sandwich composite beam structures are extensively studied using the commonly available piezoelectric materials such as polyvinylidene fluoride (PVDF) and Lead zirconate titanate (PZT-5H) (Beheshti-Aval and Lezgy-Nazargah, 2010; Komijani et al., 2014; Lezgy-Nazargah et al., 2013; Reddy and Cheng, 2001; Vidal and Polit, 2008). PVDF is a ferroelectric polymer that exhibits tailorable piezoelectric, dielectric, ferroelectric properties as well (Dang et al., 2003). Recently, a novel class of active metamaterials has been developed by exploiting the electromechanical coupling of piezoelectric materials (Singh et al., 2021). The FG hybrid composite shell with carbon nanotubes (CNTs) as reinforcement element was investigated by Thomas and Roy (2017) using the Rayleigh damping model. They reported that after the incorporation of CNTs, the frequency response of composite shells showed enhanced magnitude because of enriched stiffness and damping performance which results in a decrease in its amplitude. Abolhasani et al., (2017) first prepared graphene reinforced PVDF nanocomposite and experimentally investigated its crystallinity, polymorphism, morphology, and electrical outputs. Since 2017, the pioneering works on the emerging area of FG graphene-based composites and their structures such as beams, plates, arches, and shells are being carried out by several researchers (Naskar, 2018a; Naskar et al., 2019, 2018b). For instance, Feng et al. (2017) studied the nonlinear bending behavior of a novel class of multi-layered FG graphene platelets (GPLs)-based composite nanobeams with non-uniform distribution of GPLs along thickness direction. They found the most effective technique to decrease the deflections of beams by incorporating more GPLs in square shape with smaller amount of single graphene to its upper and bottom surfaces. Yang et al. (2018) investigated the free vibration and buckling response of FG GPLs-reinforced porous composite nanoplates based on Chebyshev-Ritz method and first-order shear deformation theory (FSDT). To attain enhanced vibration and buckling response of nanocomposite plates, a comprehensive parametric analysis was performed by considering different weight fraction, geometric parameters of GPLs nanofillers and the porosity coefficient. Zhao et al. (2020) systematically presented a brief review to study the graphene-based composites and newly FG graphene-reinforced nanocomposite using different micromechanical models. They also reviewed different theories required for investigating the mechanical analyses of FG composites structures with advantages, limitations and future technical challenges. In the case of FG graphene-based polymer composite nanoplate, Kitipornchai and his co-authors studied the free and forced vibration (Song et al., 2017), bending (Yang et al., 2017), and buckling responses (Song et al., 2018). From these studies, they have concluded that one can tailor the desired mechanical response including bending deflection, buckling, and post-buckling, as well as the natural frequency of the composite plates by altering the nonuniformity in the distribution pattern of GPLs. Based on HSDT, Shen and his co-authors investigated the nonlinear bending (Shen et al., 2017a), vibration (Chen et al., 2017), and buckling and post-buckling (Shen et al., 2017b) behavior of graphene-based layered composite plates including thermal loading. (Kiani, 2018) examined the free vibration of composite plates incorporated with GPLs to study large amplitudes with the help of iso-geometric finite element (FE) modeling. Researchers (Karsh et al., 2019; Shingare and Kundalwal, 2019, 2020; Shingare and Naskar, 2021a; Trinh et al., 2020; Vaishali et al., 2020; Naskar et al., 2017) studied the electromechanical response of hybrid graphene-based nanocomposites (GNC) including beam, plate, wire, and shell by incorporating piezoelectric graphene nanofiber in a polyimide matrix. In such studies, they assumed graphene as nanofiber and found the effect of size-dependent phenomena (piezoelectricity, flexoelectricity, and surface effect) on these non-FGM GNC structures. Using analytical and numerical models, they were able to examine the piezoelastic and dielectric properties of GNC. They showed a substantial enrichment in the structural response of GNC structures by accounting for these size-dependent properties and also revealed that one should not ignore these effects at the nanoscale. Kundalwal et al. (2020) investigated the stress transfer characteristics and mechanical properties of composites including nano- and micro-scale reinforcements via micromechanical pull-out model and molecular dynamic (MD) simulations.

In addition to piezoelectricity, flexoelectricity is also a noteworthy phenomenon, specifically in nano- and microscales (Hamdia et al., 2018; Li et al., 2021). This is the formation of electric polarization (P_i) due to a strain gradient ($\varepsilon_{\mathrm{jk,l}}$) inside all-dielectric material whether it is non-centrosymmetric (piezoelectric material) or centrosymmetric structure. Schematically, this can be expressed by the following relation: $P_i \approx \mathrm{d}_{\mathrm{ijk}}\varepsilon_{\mathrm{jk}} + \mu^{\mathrm{dir}}_{\mathrm{ijkl}}\varepsilon_{\mathrm{jk,l}}$; where $\mu^{\mathrm{dir}}_{\mathrm{ijkl}}$ and $\mathrm{d}_{\mathrm{ijk}}$ are direct flexoelectric (non-zero for all-dielectric materials) and piezoelectric constant (zero for non-piezoelectric materials), respectively (Chandratre and Sharma, 2012; Shu et al., 2019).

Sharma et al. (2021) reported the substantial enrichment in resultant coupling in the presence of flexoelectricity and piezoelectricity both in an electrically poled material sample. Besides the piezoelectric and flexoelectric effects, the surface effect is a size-dependent property that has a significant impact on the elastic response of structural building block elements. Due to the high surface-to-volume ratio, it plays a crucial part in forecasting static and dynamic characteristics of nanostructures (Gurtin and Ian Murdoch, 1975; He and Lilley, 2008; Liu and Rajapakse, 2010; Miller and Shenoy, 2000; Shenoy, 2005). For instance, Gurtin and Murdoch initially proposed a fundamental theory of surface elasticity, namely, GM surface elasticity theory in order to account for the surface effects (Gurtin and Ian Murdoch, 1975). Rajapakse and co-authors (Liu et al., 2011; Liu and Rajapakse, 2010, 2013; Sapsathiarn and Rajapakse, 2017) explored the effect of different surface parameters such as surface elasticity, surface energy, levy parameters, etc., on different structural elements subjected to different loadings (point and UDL) and boundary conditions (cantilever, simply-supported and clamped-clamped). Yan and Jiang (2012a) and Yan and Jiang (2012b) investigated the influences of surface parameters on the static bending, vibration, and buckling behavior of a non-FGM nanoplate where they mentioned two cases, traction free boundary condition and without in-plane movement of plate's mid-plane, and reported that the residual surface stress becomes more noticeable in the latter case. By using Mindlin and Kirchhoff plate theories, Ebrahimi and Hosseini (2020) studied the effect of flexoelectricity on nonlinear forced vibration of piezoelectric FG porous composite nanoplate subjected to electric voltage and external parametric excitation without considering surface effect. They also reported that electric voltage has no influence on the performance of piezoelectric and flexoelectric properties of the material on vibrational response. In this, they didn't consider the surface effects and static response of nanocomposite plates. Shingare and Naskar (2021b) studied the effect of piezoelectricity and surface on a hybrid graphene-based composite plate to study its static and dynamic responses, but didn't consider the effect of flexoelectricity. From the study of extensive literature in related fields, it is noticed that the classical continuum mechanics is not able to consider the small-scale effect of nano-scaled structures due to the absence of any material length scale parameters. Considering the inadequacies of classical continuum theories to incorporate size effects, the higher-order non-classical continuum theories, which give more precise outcomes by taking size effects into account, have been strongly suggested. Moreover, due to the time-consuming nature of MD simulation presented by Chan and Pu (2011) and Mehralian et al. (2017) and limitations of experimentation (Li et al., 2018) for determining length scale parameters, in recent years, several non-classical elasticity theories such as non-local elasticity theory, shear deformation theory, modified strain gradient elasticity theory and modified coupled stress theory (MCST) have been suggested. For instance, based on nonlocal elasticity theory of Eringen in conjunction with surface elasticity theories, Ebrahimi and Barati (2017) studied the electromechanical buckling response of non-FG flexoelectric nanoplates. They compared their results for higher buckling loads with and without considering flexoelectric effects and reported that the flexoelectric nanoplate shows enhanced results at smaller thicknesses. More recently, Ghobadi et al. (2020) and Ghobadi et al. (2021a, 2021b) developed a continuous-based thermo-electromechanic model based on assumptions of Kirchhoff plate's theory and the modified flexoelectricity theory in conjunction with the strain gradient theory in order to study the size-dependent nonlinear free vibration of FG flexoelectric nanoplate subjected to a thermo-electro-mechanical loading. They also investigated the effect of the diverse distribution of porosity on the static and nonlinear dynamic responses of a sandwich FG nanostructure. The nonlinear governing differential equations of the nanoplate and their respective boundary conditions were solved by using Hamilton's principle and variation method, and the governing equations were solved by using Galerkin's and perturbation methods. Furthermore, the advantage of modified coupled stress theory developed by Yang et al. (2002) over the earlier version of couple stress theory is that the former one needs only one material length scale parameter as compared to later which needs two parameters. Earlier, the MCST was frequently utilised for micro-scale structures, not for nanoscales. Furthermore, contrary to this, Akbarzadeh Khorshidi (2018) correctly showed that if experimental data within the relevant range is available, the material length scale parameter can be determined for micro- or nano-scaled thickness, and it is also concluded that MCST covers both micro and nano ranges if the material length scale parameter is determined in these ranges. Again, Akbarzadeh Khorshidi (2020) confirmed the conclusion of his aforementioned paper by comparing the results of MCST for two single-walled CNTs with MD simulation results by Wang and Hu (2005). Therefore, in present study, authors used the MCST as it is capable for considering the higher-order electro-mechanical coupling effects besides size effects. By taking inspiration from above mentioned work and approaches, authors proposed the MCST for advanced graphene-reinforced FG nanocomposites using the powerful frameworks of semi-analytical 'single-term extended Kantorovich method (EKM)' and 'Ritz method' for investigating the static and dynamic electromechanical responses considering flexoelectric as well as surface effects. It should be noted that the size effect is considered in this formulation based on the MCST for analyzing the anisotropic nanostructures and can also be used for isotropic structures. Besides, this formulation can also be converted into the classical plate formulation.

From a careful review of literature, it can be noticed that researchers have worked on different types of theories such as Euler Bernoulli beam, Kirchhoff's plate theory, weighted residual method, and approximated Ritz method for studying the mechanical behaviour of different structures. These methods consume significant computational time for convergence of results and hence, it is important to consider more efficient methods such as EKM for evaluating mechanical behaviour with a higher convergence rate. In 1968, reported the very effective EKM for obtaining semi-analytical solutions to 2-D elasticity problems including bivariate PDEs. Another advantage of EKM is that one can choose the priori function arbitrarily irrespective of whether it fulfills the boundary conditions of the concerned geometry or not. The iterations over the two axes are carried out in repetition till the convergence is attained, which turns out to be faster compared to Galerkin's and Ritz's methods. For instance, Kapuria and Kumari (2011, 2012, 2013) employed the powerful EKM in the 3-D elasticity problem of transversely loaded laminated structures. They also envisaged the coupled electromechanical behaviour, comprising the edge effects of single-layer piezoelectric sensors and hybrid laminates, when subjected to electromechanical loadings conditions.

With the tremendous recent advances in nano-scale manufacturing capabilities (Jang et al., 2013), while the literature categorically reveals the crucial influences of size-dependent properties such as piezoelectricity, flexoelectricity, and surface effect on the static and dynamic electromechanical behaviour of different structural elements, the aspect of effective and efficient modeling of the coupled behavior becomes a priority for better understanding of the physical behavior and subsequent engineering applications. However, the coupled electromechanical problems of functionally graded piezoelectric materials (FGPM) considering surface and flexoelectric effects in open-circuit have not been explored in a unified efficient framework so far. Therefore, the objective of the present work is to provide a unified mathematical formulation for the open-circuit electric boundary condition of the proposed composite nanostructure, as well as to analyze its size-dependent behaviors for various FGPM distributions: (i) linear distribution (LD), (ii) uniform distribution (UD) and (iii) parabolic distribution (PD). This paper hereafter is organized as: **Section 2** presents the theoretical formulation to analyze the static and dynamic behavior of FGPM nanoplates subjected to electromechanical loading considering both flexoelectric as well as surface effects. Here two different semi-analytical models such as EKM for flexoelectric and surface effects as well as Ritz method would be incorporated for developing an efficient computational framework; **Section 3** deals with the results and discussion on the effect of flexoelectricity and surface parameters on the static and dynamic behavior of FGPM nanoplates (referred to as “flexo-surface FGPM nanoplates”). **Section 4** presents the summary of the results and concluding remarks. A comprehensive overview of the current research work is systematically presented in Fig. 1. These results would offer new insights to engineer the domain configurations for tailoring the desired static and dynamic electromechanical responses of the novel graphene reinforced FG materials considering surface and flexoelectric effects. This would be demonstrated by comparison of different sets of results such as (i) conventional nanoplate (without flexo and surface effects), (ii) flexo FGPM nanoplate (considering only flexoelectric effect), and (iii) flexo-surface FGPM nanoplate (considering flexo and surface effects). Thus, the present study aims to complete a gap in our knowledge about the consideration of flexoelectric and surface effects for FGPM nanostructures.

2. Theoretical formulations

In the present section, the governing differential equations for thin square FGPM nanoplates subjected to electromechanical loading and boundary conditions are developed to study the static and dynamic responses using two different semi-analytical solution methods: (i) Extended Kantorovich method (EKM) and (ii) Ritz method, respectively. These solution approaches in the static and dynamic domains have been chosen here

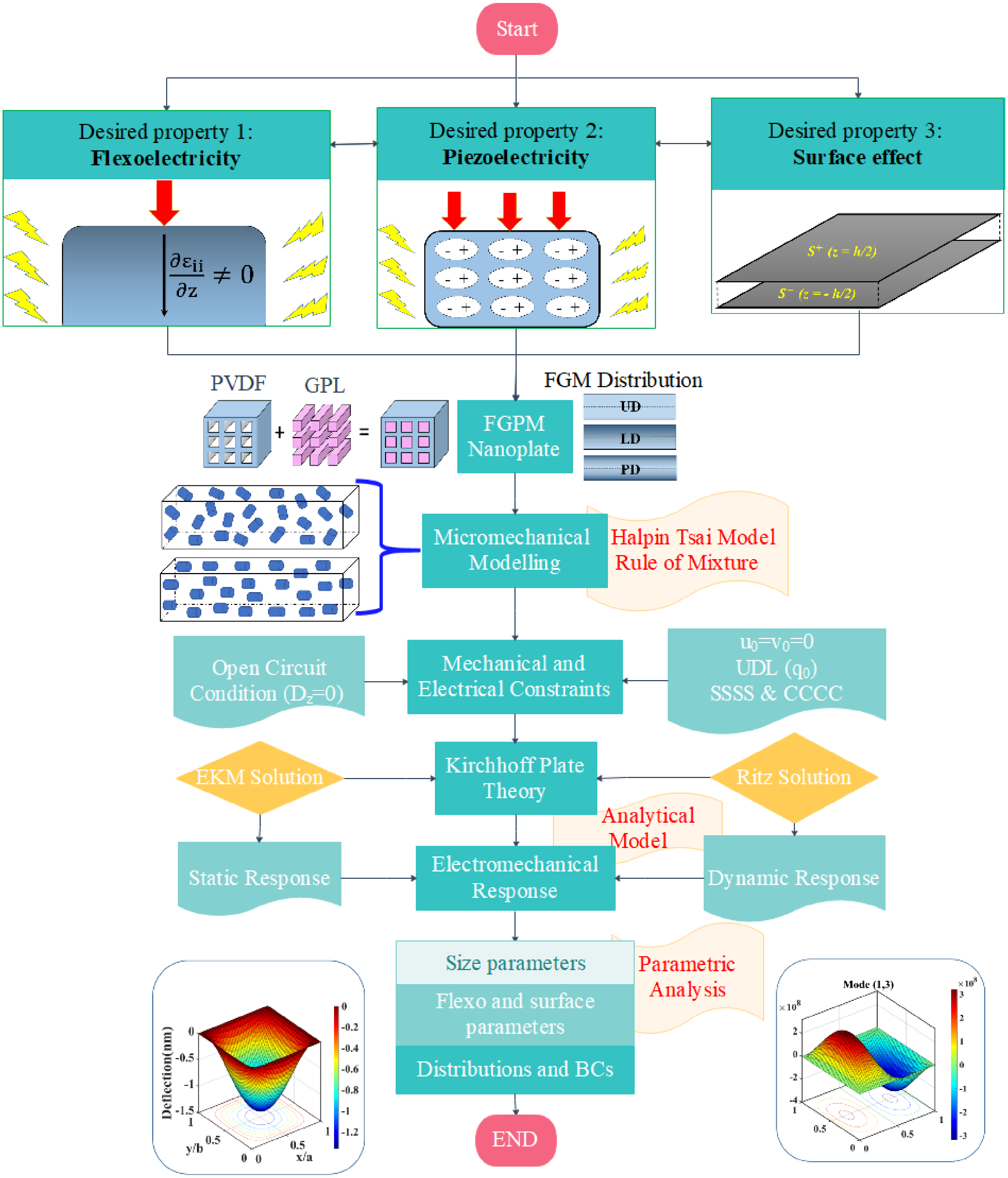

Fig. 1. Detailed flowchart of electromechanical analysis of FGPM flexo-surface nanoplates.

based on the consideration of computational convenience as per published literature (Jones and Milne, 1976; Singhatanadgid and Singhanart, 2019), which is further discussed later in this section.

2.1 Geometrical consideration

Figure 2(a) represents a thin square undeformed FGPM nanoplate of length a, width b, uniform thickness h and its associated rectangular coordinate system (x, y, z), where $z -$axis defines its out-of-plane direction and the in-plane axis $(x - y)$ is lying in the mid-plane $(z = 0)$. It is assumed that the piezoelectric polarization direction is along the z–axis. This FGPM nanoplate is subjected to a uniform transverse (downwards) loading q_0 over its upper surface and placed in the open-circuit electric boundary conditions. In the context of FGM system, the variation of material property is expected to be continuous (Vatanabe et al., 2014) and limited to the thickness direction $(\mathrm{z}-\text{axis})$.

Here the FGM system with a regular shaped (square) geometry is considered for analysis because it exhibits a more prominent flexoelectric effect due to the large strain gradient and can reduce the geometry dependency requirement of flexoelectricity (Sharma et al., 2021). In this paper, both flexoelectric and surface effects are considered. The upper $\left(\mathrm{z} = \frac{\mathrm{h}}{2}\right)$ and lower surface $\left(\mathrm{z} = -\frac{\mathrm{h}}{2}\right)$ of the plate are denoted by S^{+} and S^{-} which are schematically shown in figure 2(b). Here the whole FGPM system can be divided into two regions, the surfaces and the bulk region.

2.2 Micromechanical models – effective material properties

2.2.1 Material properties of the bulk region

The present FGPM system consists of the graphene nanoplatelets (GPLs)-based nanocomposite where a piezoelectric polymer is used as the matrix phase. Polyvinylidene fluoride (PVDF) is a good choice for this composite as it shows excellent piezoelectric and dielectric properties. The GPLs are assumed as rectangular-shaped solid reinforcement of average width w_{GPL}, length l_{GPL} and thickness t_{GPL}, where these are non-

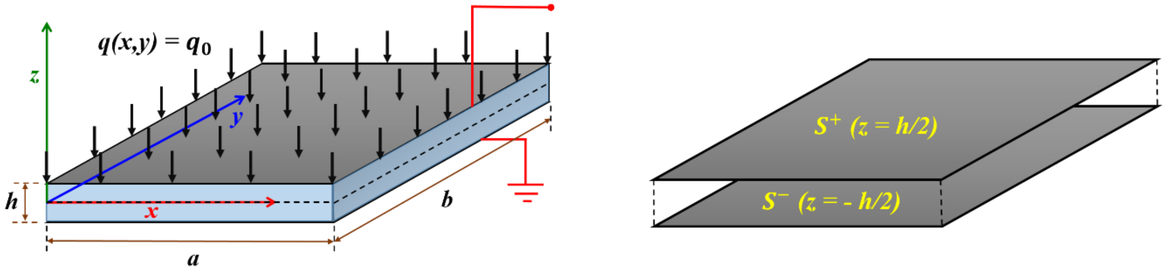

(a) (b)

Fig. 2. (a) Geometry and coordinate system of thin FGPM nanoplates under open circuit condition, **(b)** upper and lower surface of the nanoplate.

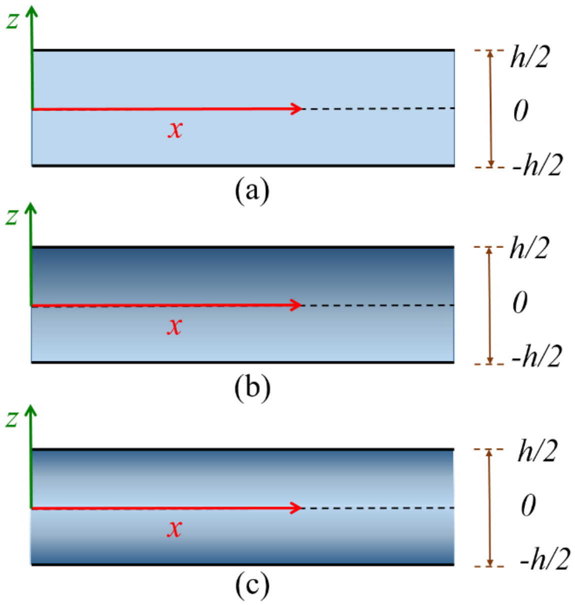

Fig. 3. Distribution of $\mathrm{W_{GPL}}$ across the thickness of FGPM nanoplates (x– z plane): **(a)** uniform, **(b)** linear and **(c)** parabolic pattern.

uniformly dispersed with varying weight fractions across the thickness of the composite plate. To determine the effective elastic properties of the present nanocomposite incorporating geometrical parameters (Shingare and Naskar, 2021a), Halpin-Tsai (HT) model is adopted whereas the effective piezoelectric and dielectric properties are determined by the rule of mixture (ROM).

In this work, three distribution patterns of GPLs are considered where the weight fraction of GPLs varies as per the following relations (Yang et al., 2017; Z. Zhao et al., 2020):

Uniform distribution (UD):
$$\mathrm{W_{GPL}(z) = 100W_{char}W_{GPL}^{t}} \tag{1a}$$

Parabolic distribution (PD):
$$\mathrm{W_{GPL}(z) = 300W_{char}}\frac{4z^2}{h^2}\mathrm{W_{GPL}^{t}} \tag{1b}$$

Linear distribution (LD):
$$\mathrm{W_{GPL}(z) = 200W_{char}}\left(\frac{\mathrm{z}}{\mathrm{h}}+\frac{1}{2}\right)\mathrm{W_{GPL}^{t}} \tag{1c}$$

where $\mathrm{W_{GPL}^{t}}$ and $\mathrm{W_{char}}$ are the total weight fraction (%) and characteristic value of GPLs weight fraction (%), respectively. These three distributions are depicted in figure 3 schematically. The total volume fraction of GPLs is calculated with the help of the following relation:

$$\mathrm{V_{GPL}(z)} = \frac{\mathrm{W_{GPL}(z)}}{\mathrm{W_{GPL}(z)} + \left(\frac{\rho_{\mathrm{GPL}}}{\rho_{\mathrm{PVDF}}}\right)(1-\mathrm{W_{GPL}(z)})} \tag{2}$$

where ρ_{GPL} and ρ_{PVDF} denote the respective mass densities of GPLs and PVDF matrix.

The elastic modulus of the system from the HT model is determined as follows (Wang et al., 2020):

$$\mathrm{E(z)} = \frac{3}{8}\mathrm{E_L} + \frac{5}{8}\mathrm{E_T} \tag{3}$$

whereas $\mathrm{E_L}$ and $\mathrm{E_T}$ indicate moduli in the longitudinal and transverse directions respectively and the values can be estimated from Eq. (4). Here, $\frac{3}{8}$ and $\frac{5}{8}$ are the reinforcing efficiency of GPLs considered in longitudinal and transverse directions, respectively.

$$\{\mathrm{E_L(z)}, \mathrm{E_T(z)}\} = \left\{\frac{1 + \xi_L^{GPL}\eta_L^{GPL}V_{GPL}(z)}{1 - \eta_L^{GPL}V_{GPL}(z)}, \frac{1 + \xi_W^{GPL}\eta_W^{GPL}V_{GPL}(z)}{1 - \eta_W^{GPL}V_{GPL}(z)}\right\}\mathrm{E_{PVDF}} \tag{4}$$

where the parameters η_L^{GPL} and η_W^{GPL} can be expressed by:

$$\{\eta_L^{GPL}, \eta_W^{GPL}\} = \left\{\frac{\left(\frac{E_{GPL}}{E_{PVDF}}\right) - 1}{\left(\frac{E_{GPL}}{E_{PVDF}}\right) + \xi_L^{GPL}}, \frac{\left(\frac{E_{GPL}}{E_{PVDF}}\right) - 1}{\left(\frac{E_{GPL}}{E_{PVDF}}\right) + \xi_W^{GPL}}\right\} \tag{5}$$

The parameters $\mathrm{E_{GPL}}$ and $\mathrm{E_{PVDF}}$ indicate the respective Young moduli of GPLs and PVDF matrix. The filler geometric factors ξ_L^{GPL} and ξ_W^{GPL} of GPLs are given by the following equation:

$$\{\xi_L^{GPL}, \xi_w^{GPL}\} = \left\{\frac{2l_{GPL}}{t_{GPL}}, \frac{2w_{GPL}}{t_{GPL}}\right\} \tag{6}$$

Due to the existence of the piezoconductive effect of graphene which is greatly dependent on its layer number (Xu et al., 2015), in the current mathematical model, it is supposed that the piezoelectric properties of GPL are α times stronger than PVDF (Mao and Zhang, 2018). Other material properties are derived from the ROM as follows:

$$\rho(z) = \rho_{GPL}V_{GPL}(z) + \rho_{PVDF}(1 - V_{GPL}(z)) \tag{7a}$$

$$\nu(z) = \nu_{GPL}V_{GPL}(z) + \nu_{PVDF}(1 - V_{GPL}(z)) \tag{7b}$$

$$[e_{3i}(z)] = \alpha[e_{3i}]^{PVDF}V_{GPL}(z) + [e_{3i}]^{PVDF}(1 - V_{GPL}(z)) \tag{7c}$$

$$[a_{ii}(z)] = \alpha[a_{ii}]^{PVDF}V_{GPL}(z) + [a_{ii}]^{PVDF}(1 - V_{GPL}(z)) \tag{7d}$$

where ν, e_{3i} $(i = 1, 2)$, a_{ii} $(i = 3)$ and α are the Poisson's ratio, coupling coefficient, electric permittivity, and piezoelectric multiple, respectively. Regarding the intrinsic flexoelectric coefficient of the present FGPM composite system, due to the unavailability of sufficient literature and difficulties in the experimental determination of f_{14} (Shu et al., 2014) , we assume it constant throughout the bulk region under the assumption of crystal with cubic symmetry ($f_{3223} = f_{3113} = f_{14}$). Also due to the incorporation of reinforcement elements (e.g. GPLs) in the PVDF matrix, there will be an increase in the value of f_{14} (Hu et al., 2018). This is why the flexoelectric coefficient (f_{14}) is set within a range in the current model. The range of its values is taken as the same as that of the other two components of the flexoelectric tensor (i.e., f_{11} and f_{12}) of PVDF-based polymers (Baskaran et al., 2011; Zhou et al., 2017). This range is also mentioned in section 3.2. However, note that the analytical model developed here is equally applicable for both varying and constant flexoelectric systems.

2.2.2 Material properties concerning the surface layers (S^+ and S^-)

Due to lack of proper atomistic experiments and to deal with the problem of zero thickness outer layers, one characteristic length (ξ_c) is assumed to estimate the surface material constants of the present FGPM system. The surface constants of the upper and lower surface layers are related to their corresponding bulk constants by the following relations (Pan et al., 2011; Shingare and Kundalwal, 2020):

$$\text{Upper surface } (S^+): \quad c_{ij}^{+} = \xi_c \,.\, c_{ij}\left(z = \frac{h}{2}\right),\ e_{ij}^{+} = \xi_c \,.\, e_{ij}\left(z = \frac{h}{2}\right) \tag{8a}$$

$$\text{Lower surface } (S^-): \quad c_{ij}^{-} = \xi_c \,.\, c_{ij}\left(z = -\frac{h}{2}\right), e_{ij}^{-} = \xi_c \,.\, e_{ij}\left(z = -\frac{h}{2}\right) \tag{8b}$$

From Eq. (8), it is evident that in the FGPM system, the surface properties of the upper and lower surface are different (Hosseini et al., 2017). Here, the value of the residual surface stress σ_{xy}^{0} is considered as zero (Zhang et al., 2012).

2.3 Constitutive relations of bulk and surface layer

2.3.1 Bulk region

To incorporate the flexoelectricity phenomena along with its inbuilt piezoelectricity within the bulk region, an extended linear theory of piezoelectricity is adopted under the assumption of infinitesimal deformation. Hence, the general expression of the electric Gibbs free energy density function for the bulk region can be given as follows (Liang et al., 2013):

$$U_{bulk} = -\frac{1}{2}a_{kl}E_k E_l + \frac{1}{2}c_{ijkl}\varepsilon_{ij}\varepsilon_{kl} - e_{kij}E_k\varepsilon_{ij} - f_{ijkl}E_i\varepsilon_{jk,l} + r_{ijklm}\varepsilon_{ij}\varepsilon_{kl,m} + \frac{1}{2}g_{ijklmn}\varepsilon_{ij,k}\varepsilon_{lm,n} \tag{9}$$

where a_{kl}, c_{ijkl}, e_{kij}, and f_{ijkl} are the element of material property tensors – permittivity (rank 2 tensor), elastic stiffness (rank 4 tensor), piezoelectric coupling (rank 3 tensor), and flexocoupling (rank 4 tensor), respectively. E and ε are the electric field vector and strain component, respectively. In Eq. (9), tensor f couples strain gradient and electric field whereas r and g are higher-order coupling terms which couple strain and its strain gradient, and strain gradient and strain gradient, respectively. Here the comma in the subscript of ε indicates its differentiation with respect to one spatial variable. Under the aforementioned assumption, the higher-order coupling terms r and g are neglected to simplify the current formulation. Following generalized constitutive relations for the bulk region are derived using Eq. (9).

$$\sigma_{\mathrm{ij}}=\frac{\partial \mathrm{U}_{\mathrm{bulk}}}{\partial \varepsilon_{\mathrm{ij}}}=\mathrm{c}_{\mathrm{ijkl}}\varepsilon_{\mathrm{kl}}-\mathrm{e}_{\mathrm{kij}}\mathrm{E}_{\mathrm{k}} \tag{10a}$$

$$\sigma_{\mathrm{jkl}}=\frac{\partial \mathrm{U}_{\mathrm{bulk}}}{\partial \varepsilon_{\mathrm{jk,l}}}=-\mathrm{f}_{\mathrm{ijkl}}\mathrm{E}_{\mathrm{i}} \tag{10b}$$

$$\mathrm{D}_{\mathrm{k}}=-\frac{\partial \mathrm{U}_{\mathrm{bulk}}}{\partial \mathrm{E}_{\mathrm{k}}}=\mathrm{a}_{\mathrm{kl}}\mathrm{E}_{\mathrm{l}}+\mathrm{e}_{\mathrm{kij}}\varepsilon_{\mathrm{ij}}+\mathrm{f}_{\mathrm{klmn}}\varepsilon_{\mathrm{lm,n}} \tag{10c}$$

where σ_{ij} and $\varepsilon_{\mathrm{ij}}$ are the classical stress and strain tensor. σ_{jkl} is the hyper stress tensor generated due to consideration of flexoelectricity; $\varepsilon_{\mathrm{jk,l}}$ is the higher-order strain gradient tensor. $\mathrm{f}_{\mathrm{ijkl}}$ denotes fourth-order flexocoupling tensor; D_{k} and E_{i} are the electric displacement and electric field vector. a_{kl} and $\mathrm{e}_{\mathrm{kij}}$ denote the second-order permittivity and third-order piezoelectric tensor. In contrast to the conventional piezoelectric relation in Eq. (10c), it is observed that there is also a contribution of flexoelectricity in the electric displacement of the nanoplate.

While considering the flexoelectric effect, Shu et al. (2011) reported the direct flexoelectric coefficient tensor for a cubic crystal, and these can be expressed as:

$$\mathrm{f}_{3\times 18}=\begin{pmatrix} \mathrm{f}_{11} & 0 & 0 & \mathrm{f}_{14} & 0 & 0 & \mathrm{f}_{14} & 0 & 0 & 0 & \mathrm{f}_{111} & 0 & 0 & 0 & \mathrm{f}_{111} & 0 & 0 & 0 \\ 0 & \mathrm{f}_{14} & 0 & 0 & \mathrm{f}_{11} & 0 & 0 & \mathrm{f}_{14} & 0 & \mathrm{f}_{111} & 0 & 0 & 0 & 0 & 0 & 0 & 0 & \mathrm{f}_{111} \\ 0 & 0 & \mathrm{f}_{14} & 0 & 0 & \mathrm{f}_{14} & 0 & 0 & \mathrm{f}_{11} & 0 & 0 & 0 & \mathrm{f}_{111} & 0 & 0 & 0 & \mathrm{f}_{111} & 0 \end{pmatrix}$$

where $\mathrm{f}_{1111}=\mathrm{f}_{2222}=\mathrm{f}_{3333}=\mathrm{f}_{11}, \mathrm{f}_{1133}=\mathrm{f}_{2233}=\mathrm{f}_{1122}=\mathrm{f}_{2121}=\mathrm{f}_{3232}=\mathrm{f}_{3131}=\mathrm{f}_{111},$ $\mathrm{f}_{1221}=\mathrm{f}_{1331}=\mathrm{f}_{2112}=\mathrm{f}_{2332}=\mathrm{f}_{3223}=\mathrm{f}_{3113}=\mathrm{f}_{14}$. In addition to this, as the thickness of the proposed FGPM plate is considered as very small as compared to length and width, the electric displacement and electric field in the x- and y- directions are considered as zero ($E_x=E_y=0$; $D_x=D_y=0$). This indicates the electric field and electric displacement to be present only along the z-direction ($E_z=D_z\neq 0$) and the strain variations are also considered along z-direction only i.e., $\varepsilon_{\mathrm{xx,z}}$ and $\varepsilon_{\mathrm{yy,z}}$. In other words, in Eq. (10c), 'k' and 'n' will be '3' and 'l' and 'm' will be either 1 or 2 (i.e., $\mathrm{f}_{3223}=\mathrm{f}_{3113}=\mathrm{f}_{14}$). So, it is evident that the flexoelectric coefficients except f_{14} will be zero ($f_{14}\neq 0$). As the present thin FGPM plate is under the 2D assumption, all strains must be in-plane only. Therefore, e_{311} and e_{322} will be non-zero ($e_{311},\ e_{322}\neq 0$). Consequently, the second-order permittivity tensor is also considered in z-direction only ($a_{11},\ a_{22}=0; a_{33}\neq 0$). Later the values of non-zero coefficients are given in Table 4 for the present study.

For the present FGPM system, Eq. (10) can be rewritten by considering bi-subscript notations (Wang and Li, 2021) and cubic crystal symmetry as follows:

$$\sigma_{\mathrm{xx}}=\mathrm{c}_{11}(\mathrm{z})\varepsilon_{\mathrm{xx}}+\mathrm{c}_{12}(\mathrm{z})\varepsilon_{\mathrm{yy}}-\mathrm{e}_{31}(\mathrm{z})\mathrm{E}_{\mathrm{z}} \tag{11a}$$

$$\sigma_{yy} = c_{12}(z)\varepsilon_{xx} + c_{22}(z)\varepsilon_{yy} - e_{32}(z)E_z \tag{11b}$$

$$\sigma_{xy} = c_{66}(z)\gamma_{xy} = 2c_{66}(z)\varepsilon_{xy} \tag{11c}$$

$$\sigma_{xxz} = -f_{14}(z)E_z \tag{11d}$$

$$\sigma_{yyz} = -f_{14}(z)E_z \tag{11e}$$

$$D_z = a_{33}(z)E_z + e_{31}(z)\varepsilon_{xx} + e_{32}(z)\varepsilon_{yy} + f_{14}(z)\left(\varepsilon_{xx,z} + \varepsilon_{yy,z}\right) \tag{11f}$$

where ε_{xx}, ε_{yy} and ε_{xy} are classical in-plane strains. In this, all material constants are considered as the functions of *z* due to the thickness-wise FGM system under consideration.

2.3.2 Surface layers ($S^+$and S^-)

Similar to the bulk region, the general constitutive relations for the surfaces (S^+ and S^-) of FGPM nanoplates can be derived from the surface energy density function U_{sur} which are given as follows (Huang and Yu, 2006):

$$\sigma_{ij}^{s} = \frac{\partial U_{sur}}{\partial \varepsilon_{ij}} = \sigma_{ij}^{0} + c_{ijkl}^{s}\varepsilon_{kl} - e_{kij}^{s}E_k \tag{12a}$$

$$D_k^{s} = -\frac{\partial U_{sur}}{\partial E_k} = D_k^{0} + a_{kl}^{s}E_l + e_{kij}^{s}\varepsilon_{ij} \tag{12b}$$

wherein σ_{ij}^0 and D_k^0 are the surface residual stress and surface electric field, respectively. Here the surface quantities are indicated by superscript ‘s’. According to Zhang et al. (2013), the equations of strain (ε_{kl}) and electric field (E_k) in case of surface effects are the same as that of the bulk one. Based on the present FGPM system, one can rewrite the surface stresses as follows:

$$\sigma_{xx}^{s} = \sigma^0 + c_{11}^{s}(z)\varepsilon_{xx} + c_{12}^{s}(z)\varepsilon_{yy} - e_{31}^{s}(z)E_z \tag{13a}$$

$$\sigma_{yy}^{s} = \sigma^0 + c_{21}^{s}(z)\varepsilon_{xx} + c_{22}^{s}(z)\varepsilon_{yy} - e_{32}^{s}(z)E_z \tag{13b}$$

$$\sigma_{xy}^{s} = 2c_{66}^{s}(z)\varepsilon_{xy} \tag{13c}$$

$$D_z^{s} = 0 \tag{13d}$$

2.4 Governing equations for static and dynamic analysis

As the present model is under open-circuit (sensor type) condition, the electric displacement (D_z) on the surfaces of FGPM nanoplate is zero (Zhang et al., 2013) and it can be achieved if the top and bottom-most surfaces are insulated (Wang and Zhou, 2013). It also satisfies Gauss law of dielectrics $\left(\mathrm{div}\,\vec{\mathrm{D}} = \mathrm{Q}_{\mathrm{free}}\right)$ where free electric charge density $(\mathrm{Q}_{\mathrm{free}})$ is zero. From Eq. (11f), for the zero electric displacement $(\mathrm{D}_{\mathrm{z}} = 0)$, the internal electric field $(\mathrm{E}_{\mathrm{z}})$ can be expressed as follows:

$$\mathrm{E}_{\mathrm{z}} = \frac{1}{\mathrm{a}_{33}(\mathrm{z})}\left[\mathrm{e}_{31}(\mathrm{z})\varepsilon_{\mathrm{xx}} + \mathrm{e}_{32}(\mathrm{z})\varepsilon_{\mathrm{yy}} + \mathrm{f}_{14}(\mathrm{z})(\varepsilon_{\mathrm{xx,z}} + \varepsilon_{\mathrm{yy,z}})\right] \tag{14}$$

The same electric field relation as above is also applicable for the surface constitutive equations.

In this mathematical formulation, the classical Kirchhoff plate theory is used for the thin FGPM nanoplate. As mentioned in the existing literature (Yan and Jiang, 2012a), to investigate the surface effect effectively, the mid-plane extensional deformations $(\mathrm{u}_0, \mathrm{v}_0)$ are constrained to zero. The displacement fields can be expressed as:

$$\mathrm{u}(\mathrm{x},\mathrm{y},\mathrm{z},\mathrm{t}) = -\mathrm{z}\frac{\partial \mathrm{w}_0}{\partial \mathrm{x}} \tag{15a}$$

$$\mathrm{v}(\mathrm{x},\mathrm{y},\mathrm{z},\mathrm{t}) = -\mathrm{z}\frac{\partial \mathrm{w}_0}{\partial \mathrm{y}} \tag{15b}$$

$$\mathrm{w}(\mathrm{x},\mathrm{y},\mathrm{z},\mathrm{t}) = \mathrm{w}_0(\mathrm{x},\mathrm{y},\mathrm{t}) \tag{15c}$$

Neglecting Von-Karmen non-linear terms in strain formulae, the following linear strain-displacement relations and internal electric field are derived from Eq. (14) and (15):

$$\varepsilon_{\mathrm{xx}} = \frac{\partial \mathrm{u}}{\partial \mathrm{x}} = -\mathrm{z}\frac{\partial^2 \mathrm{w}_0}{\partial \mathrm{x}^2} = \mathrm{z}\varepsilon_{\mathrm{xx}}^1 \tag{16a}$$

$$\varepsilon_{\mathrm{yy}} = \frac{\partial \mathrm{v}}{\partial \mathrm{y}} = -\mathrm{z}\frac{\partial^2 \mathrm{w}_0}{\partial \mathrm{y}^2} = \mathrm{z}\varepsilon_{\mathrm{yy}}^1 \tag{16b}$$

$$\varepsilon_{\mathrm{zz}} = \frac{\partial \mathrm{w}}{\partial \mathrm{z}} = 0 \tag{16c}$$

$$\gamma_{\mathrm{xy}} = 2\varepsilon_{\mathrm{xy}} = \frac{\partial \mathrm{u}}{\partial \mathrm{y}} + \frac{\partial \mathrm{v}}{\partial \mathrm{x}} = -2\mathrm{z}\frac{\partial^2 \mathrm{w}_0}{\partial \mathrm{x}\,\partial \mathrm{y}} = \mathrm{z}\varepsilon_{\mathrm{xy}}^1 \tag{16d}$$

$$\varepsilon_{\mathrm{xz}} = \varepsilon_{\mathrm{yz}} = 0 \tag{16e}$$

$$\varepsilon_{\mathrm{xx,z}} = \frac{\partial \varepsilon_{\mathrm{xx}}}{\partial \mathrm{z}} = -\frac{\partial^2 \mathrm{w}_0}{\partial \mathrm{x}^2} = \varepsilon_{\mathrm{xx}}^1 \tag{16f}$$

$$\varepsilon_{\mathrm{yy,z}} = \frac{\partial \varepsilon_{\mathrm{yy}}}{\partial \mathrm{z}} = -\frac{\partial^2 \mathrm{w}_0}{\partial \mathrm{y}^2} = \varepsilon_{\mathrm{yy}}^1 \tag{16g}$$

$$\mathrm{E}_{\mathrm{z}} = -\left[\mathrm{f}_{1\mathrm{z}}(\mathrm{z})\varepsilon_{\mathrm{xx}}^1 + \mathrm{f}_{2\mathrm{z}}(\mathrm{z})\varepsilon_{\mathrm{yy}}^1\right] \tag{16h}$$

where $\varepsilon^1_{xx} = -\frac{\partial^2 w_0}{\partial x^2}$, $\varepsilon^1_{yy} = -\frac{\partial^2 w_0}{\partial y^2}$, $\varepsilon^1_{xy} = -2\frac{\partial^2 w_0}{\partial x\,\partial y}$, $f_{1z}(z) = \frac{(ze_{31}(z)+f_{14}(z))}{a_{33}(z)}$ and $f_{2z}(z) = \frac{(ze_{32}(z)+f_{14}(z))}{a_{33}(z)}$. Equations (16c) and (16e) are found in coherence with the Kirchhoff hypothesis (Reddy, 2003).

The governing equations for the present FGPM system are achieved from the principle of virtual displacements that can be given as follows:

$$\int_{t_i}^{t_f} [-(\delta U_b + \delta U_s) + \delta K + \delta W_{ext}]\, dt = 0 \tag{17}$$

The virtual strain energy (δU_b) for the bulk region is expressed as follows:

$$\begin{aligned}\delta U_b &= \int_0^a \int_0^b \int_{-\frac{h}{2}}^{\frac{h}{2}} \left(\sigma_{xx}\delta\varepsilon_{xx} + \sigma_{yy}\delta\varepsilon_{yy} + \sigma_{xy}\delta\gamma_{xy} + \sigma_{xxz}\delta\varepsilon_{xx,z} + \sigma_{yyz}\delta\varepsilon_{yy,z}\right) dxdydz \\ &= \int_0^a \int_0^b \left[(M_{xx} + N_{xxz})\delta\varepsilon^1_{xx} + (M_{yy} + N_{yyz})\delta\varepsilon^1_{yy} + 2M_{xy}\delta\varepsilon^1_{xy}\right] dxdy \end{aligned} \tag{18}$$

The virtual strain energy (δU_s) considering both the surface layers can be written as follows:

$$\begin{aligned}\delta U_s &= \iint_{S^+} \left(\sigma^+_{xx}\delta\varepsilon_{xx} + \sigma^+_{yy}\delta\varepsilon_{yy} + \sigma^+_{xy}\delta\gamma_{xy}\right) dS^+ + \iint_{S^-} \left(\sigma^-_{xx}\delta\varepsilon_{xx} + \sigma^-_{yy}\delta\varepsilon_{yy} + \sigma^-_{xy}\delta\gamma_{xy}\right) dS^- \\ &= \int_0^a \int_0^b \left[(M^+_{xx} + M^-_{xx})\delta\varepsilon^1_{xx} + \left(M^+_{yy} + M^-_{yy}\right)\delta\varepsilon^1_{yy} + 2\left(M^+_{xy} + M^-_{xy}\right)\delta\varepsilon^1_{xy}\right] dxdy \end{aligned} \tag{19}$$

The virtual work done by the externally applied uniform transverse load q_0 and loads induced by the traction jump and in-plane forces (Yan and Jiang, 2012; Zhang et al., 2014) can be written as follows:

$$\begin{aligned}\delta W_{ext} = \int_0^a \int_0^b \Big[\, & q(x,y)\delta w_0 - (N_{xx} + N^+_{xx} + N^-_{xx})w_{0,x}\,\delta w_{0,x} - \left(N_{yy} + N^+_{yy} + N^-_{yy}\right)w_{0,y}\delta w_{0,y} - (N_{xy} + N^+_{xy} \\ & + N^-_{xy})(w_{0,x}\,\delta w_{0,y} + w_{0,y}\,\delta w_{0,x})\Big]\, dxdy \end{aligned} \tag{20}$$

Finally, the virtual kinetic energy considering the motions in all three directions is expressed in the following equation. Though we have shown all three directions for generality, only vibrational motion in the transverse plane of the nanoplate is considered in the final results.

$$\begin{aligned}\delta K &= \int_0^a \int_0^b \int_{-\frac{h}{2}}^{\frac{h}{2}} \rho(\dot{u}\delta\dot{u} + \dot{v}\delta\dot{v} + \dot{w}\delta\dot{w})\, dxdydz \\ &= \int_0^a \int_0^b \left[\, I_0\dot{w}_0\delta\dot{w}_0 + I_2\dot{w}_{0,x}\delta\dot{w}_{0,x} + I_2\dot{w}_{0,y}\delta\dot{w}_{0,y}\,\right] dxdy \end{aligned} \tag{21}$$

where I_0 and I_2 are the mass inertia terms and $\mathrm{N}_{\mathrm{ij}}, \mathrm{M}_{\mathrm{ij}}, \mathrm{M}_{\mathrm{ij}}^{\pm}, \mathrm{N}_{\mathrm{ij}}^{\pm}, \mathrm{N}_{\mathrm{ijk}}$ are the function resultants (stress and moment) whose definitions are given as follows:

$$\{\mathrm{N}_{\mathrm{ij}}, \mathrm{M}_{\mathrm{ij}}\} = \int_{-\frac{h}{2}}^{\frac{h}{2}} \{\sigma_{\mathrm{ij}}, z\sigma_{\mathrm{ij}}\} dz$$

$$\{\mathrm{N}_{\mathrm{ij}}^{\pm}, \mathrm{M}_{\mathrm{ij}}^{\pm}\} = \left(\sigma_{\mathrm{ij}}^{\pm}, z\sigma_{\mathrm{ij}}^{\pm}\right)_{z=\pm\frac{h}{2}}$$

$$\mathrm{N}_{\mathrm{ijk}} = \int_{-\frac{h}{2}}^{\frac{h}{2}} \sigma_{\mathrm{ijk}}\, dz$$

By substituting Eq. (16) in the aforementioned resultants, the following matrix is derived.

$$\begin{pmatrix} \mathrm{M}_{xx} \\ \mathrm{M}_{yy} \\ \mathrm{M}_{xy} \\ \mathrm{N}_{xx} \\ \mathrm{N}_{yy} \\ \mathrm{N}_{xy} \\ \mathrm{M}_{xx}^{\pm} \\ \mathrm{M}_{yy}^{\pm} \\ \mathrm{M}_{xy}^{\pm} \\ \mathrm{N}_{xx}^{\pm} \\ \mathrm{N}_{yy}^{\pm} \\ \mathrm{N}_{xy}^{\pm} \\ \mathrm{N}_{xxz} \\ \mathrm{N}_{yyz} \end{pmatrix} = \begin{pmatrix} 0 & \mathrm{A}_{11} & \mathrm{A}_{12} & 0 \\ 0 & \mathrm{A}_{21} & \mathrm{A}_{22} & 0 \\ 0 & 0 & 0 & 2\mathrm{A}_{66} \\ 0 & \mathrm{B}_{11}^{\pm} & \mathrm{B}_{12}^{\pm} & 0 \\ 0 & \mathrm{B}_{21}^{\pm} & \mathrm{B}_{22}^{\pm} & 0 \\ 0 & 0 & 0 & 2\mathrm{B}_{66} \\ \mathrm{A}_{01}^{\pm} & \mathrm{A}_{11}^{\pm} & \mathrm{A}_{21}^{\pm} & 0 \\ \mathrm{A}_{02}^{\pm} & \mathrm{A}_{12}^{\pm} & \mathrm{A}_{22}^{\pm} & 0 \\ \mathrm{A}_{0}^{\pm} & 0 & 0 & \mathrm{A}^{\pm} \\ \mathrm{B}_{01}^{\pm} & \mathrm{B}_{11}^{\pm} & \mathrm{B}_{21}^{\pm} & 0 \\ \mathrm{B}_{02}^{\pm} & \mathrm{B}_{12}^{\pm} & \mathrm{B}_{22}^{\pm} & 0 \\ \mathrm{B}_{0}^{\pm} & 0 & 0 & \mathrm{B}^{\pm} \\ 0 & \mathrm{A}_{11}^{f} & \mathrm{A}_{21}^{f} & 0 \\ 0 & \mathrm{A}_{11}^{f} & \mathrm{A}_{21}^{f} & 0 \end{pmatrix} \begin{pmatrix} 1 \\ \varepsilon_{xx}^{1} \\ \varepsilon_{yy}^{1} \\ \varepsilon_{xy}^{1} \end{pmatrix} \tag{22}$$

In Eq. (22), the stiffness coefficients and their algebraic expressions are given in **Appendix A**. Now, if we substitute Eqs. (18), (19), (20) and (21) into the Hamilton Eq. (17) and apply the principles of variational calculus, the following governing equation of the present FGPM system incorporating both flexoelectricity and surface effect can be derived.

$$\frac{\partial^2 \mathrm{M}_{xx}^*}{\partial x^2} + \frac{\partial^2 \mathrm{M}_{yy}^*}{\partial y^2} + 2\frac{\partial^2 \mathrm{M}_{xy}^*}{\partial x\, \partial y} + \frac{\partial^2 \mathrm{N}_{xxz}}{\partial x^2} + \frac{\partial^2 \mathrm{N}_{yyz}}{\partial y^2} + q_0 + \mathrm{N}_{xx}^* \frac{\partial^2 w_0}{\partial x^2} + \mathrm{N}_{yy}^* \frac{\partial^2 w_0}{\partial y^2} + 2\mathrm{N}_{xy}^* \frac{\partial^2 w_0}{\partial x\, \partial y} - \mathrm{I}_0 \ddot{w}_0 + \mathrm{I}_2\left(\ddot{w}_{0,xx} + \ddot{w}_{0,yy}\right) = 0 \tag{23}$$

Here, $\mathrm{M}_{\mathrm{ij}}^*$, $\mathrm{N}_{\mathrm{ij}}^*$ $(\mathrm{i}, \mathrm{j} = x, y)$ are obtained as follows:

$$\mathrm{M}_{\mathrm{ij}}^* = \mathrm{M}_{\mathrm{ij}} + \mathrm{M}_{\mathrm{ij}}^{+} + \mathrm{M}_{\mathrm{ij}}^{-},$$

$$N_{ij}^{*} = N_{ij} + N_{ij}^{+} + N_{ij}^{-}.$$

2.5 Solution methodology based on EKM and Ritz approach

In the present study, two semi-analytical solution methods are adopted for getting the solutions of the governing equation (23) which are the single-term extended Kantorovich method (EKM) and the Ritz method. These two methods are applied separately for the static and dynamic cases of FGPM nanoplates considering flexoelectricity as well as surface effects, and the results are validated in later sections. For the static analysis, the reason for selecting the EKM approach is its accuracy and rapid convergence rate. Its solution is also independent of the initially chosen functions. The traditional Navier approach can only be applied for all edges simply-supported (SSSS) plate whereas, the Levy method needs at least two simply supported edges of the concerned plate. In the Ritz and Galerkin method, the final solutions are dependent on initial guess (algebraic polynomials or basis) functions. It would be found in later sections of this paper that for a square thin plate $(a/h\ \geq 20)$ under the 2D assumption, a single-term EKM solution is sufficient to provide accurate results. On the other hand, the dynamic analysis is performed using the Ritz approach instead of EKM because the EKM method is computationally more intensive than other methods due to the existence of several vibrational frequencies of any continuous system and the presence of symmetric and antisymmetric vibration modes in many cases (Singhatanadgid and Singhanart, 2019). In the dynamic scenario, in each iteration of EKM there exists two unknown variables (second unknown single variable function and eigenfrequency) in the ODE obtained after substituting the first known priori function. To resolve this, we also have to take into consideration the symmetry and antisymmetry conditions about one direction of the structure and for that its final closed-form solution is dependent on the mode of vibration whether it is symmetric or antisymmetric(Jones and Milne, 1976). As in this paper, the focus is given to the analysis of the behavioural aspects of FGM nanoplate of different distributions within a semi-analytical framework, Ritz method is preferred in the dynamic scenarios. Before discussing the mathematical formulations of the analytical approaches, the boundary conditions and their mathematical representation need to be mentioned as both the techniques are based on the geometric and essential boundary conditions of the problem. We considered SSSS and clamped-clamped (CCCC) conditions for square plates which are schematically shown in figure 4.

2.5.1 Static analysis based on EKM

Substituting all the stiffness coefficients of Eq. (22) and strain-displacement relations of Eq. (16) into the governing equation (23), the following simplified form of Eq.(23) in terms of displacement can be written:

$$H_1 \frac{\partial^4 w_0}{\partial x^4} + H_2 \frac{\partial^4 w_0}{\partial y^4} + H_3 \frac{\partial^4 w_0}{\partial x^2\, \partial y^2} + H_4 \left(\frac{\partial^2 w_0}{\partial x^2}\right)^2 + H_5 \left(\frac{\partial^2 w_0}{\partial y^2}\right)^2 + H_6 \left(\frac{\partial^2 w_0}{\partial x^2}\right)\left(\frac{\partial^2 w_0}{\partial y^2}\right)$$

$$+H_7\left(\frac{\partial^2 w_0}{\partial x\,\partial y}\right)^2 - H_8\left(\frac{\partial^2 w_0}{\partial x^2}\right) - H_9\left(\frac{\partial^2 w_0}{\partial y^2}\right) - H_{10}\left(\frac{\partial^2 w_0}{\partial x\,\partial y}\right) - q_0 + I_0\ddot{w}_0 = 0 \tag{24}$$

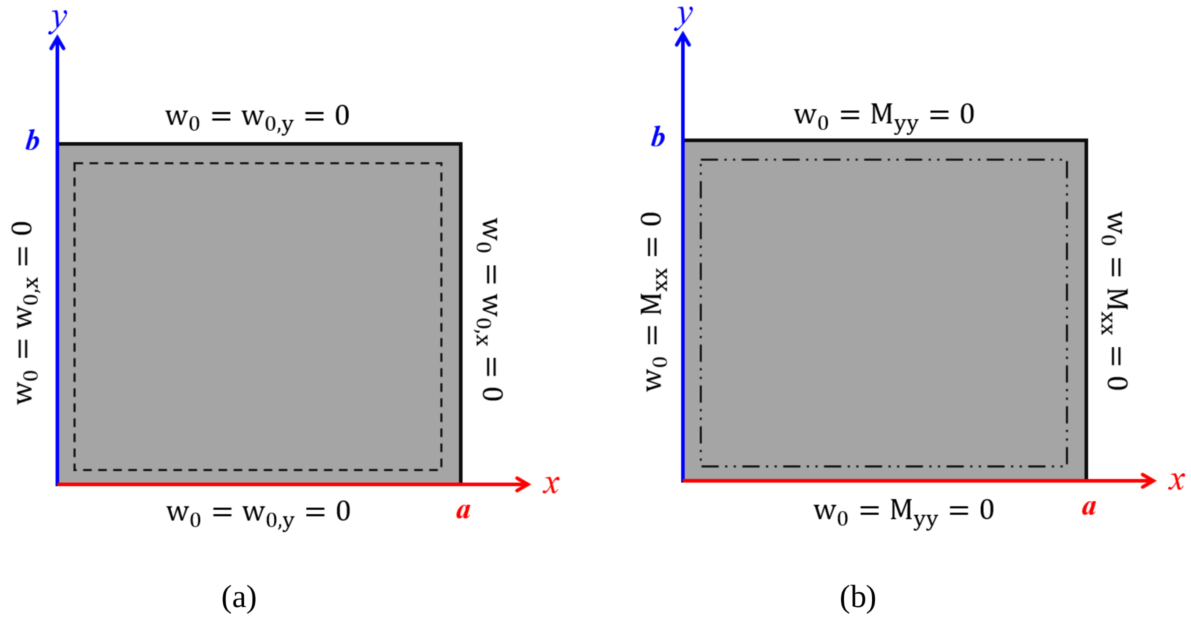

Fig. 4. FGPM nanoplates subjected to mechanical boundary conditions: **(a)** CCCC and **(b)** SSSS.

In Eq. (24), all the coefficients (H_i) of each term and their algebraic expressions are given in **Appendix B**. It is observed that Eq. (24) is non-linear in nature. Under infinitesimal deformation assumptions and to linearize the calculation process, we have neglected these four non-linear terms (H_4, H_5, H_6 and H_7) in further calculations. However, mathematical error due to neglecting the non-linearities becomes minimal if symmetrical distributions of FGM and non-flexoelectric ($f_{14} \approx 0$) surface nanoplate is considered. For instance, it is observed from the present model that in the absence of f_{14}, the magnitudes of H_4, H_5, H_6 and H_7 are zero for UD and PD distribution whereas it is in the order of 10^{-6} for LD distribution. The magnitudes become more as plate thickness increases. To account for this, the results and discussions in section 3 are mostly focused on thicknesses and distributions (UD and PD) within a reasonable range. The following equation is the weak form of nanoplate under bending which is used in the EKM method:

$$\int_0^a\int_0^b \left[\begin{array}{c} H_1\dfrac{\partial^4 w_0}{\partial x^4} + H_2\dfrac{\partial^4 w_0}{\partial y^4} + H_3\dfrac{\partial^4 w_0}{\partial x^2\,\partial y^2} - H_8\left(\dfrac{\partial^2 w_0}{\partial x^2}\right) \\ -H_9\left(\dfrac{\partial^2 w_0}{\partial y^2}\right) - H_{10}\left(\dfrac{\partial^2 w_0}{\partial x\,\partial y}\right) - q_0 \end{array}\right]\delta w_0\,dxdy = 0 \tag{25}$$

In single-term EKM, first, it is essential to assume a solution into two bivariate functions for the Eq. (25) in a separable form which is shown below:

$$w_0(x, y) = f(x).g(y) \tag{26}$$

Here either f(x) or g(y) is taken as a priori function. To start the first iteration, in the first step, a function $g_1(y)$ is chosen as priori for g(y). Another advantage of the EKM is that one can choose this priori function arbitrarily irrespective of whether it satisfies the boundary conditions of the problem or not. Now, if the updated $w_0(=f.g_1)$ function is substituted into the weak form (Eq. 25), one ordinary differential equation (ODE) of f(x) will be obtained which can be solved using any standard method of differential calculus. Following is the ODE and its associated boundary conditions after the first step.

$$\int_0^a \left[\int_0^b \left(H_1 g_1(y)\frac{\partial^4 f(x)}{\partial x^4} + H_2 f(x)\frac{\partial^4 g_1(y)}{\partial y^4} + H_3\left(\frac{\partial^2 f(x)}{\partial x^2}\right)\left(\frac{\partial^2 g(y)}{\partial y^2}\right) - H_8\, g_1(y)\left(\frac{\partial^2 f(x)}{\partial x^2}\right) - H_9 f(x)\left(\frac{\partial^2 g_1(y)}{\partial y^2}\right) - H_{10}\left(\frac{\partial f(x)}{\partial x}\right)\left(\frac{\partial g(y)}{\partial y}\right) - q_0\right) g_1(y) dy\right] \delta f(x) dx = 0 \tag{27}$$

From Eq. (27), the following ODE of f(x) is obtained:

$$K_{11}\frac{\partial^4 f}{\partial x^4} + K_{21} f + K_{31}\frac{\partial^2 f}{\partial x^2} - K_{41}\left(\frac{\partial^2 f}{\partial x^2}\right) - K_{51} f - K_{61}\left(\frac{\partial f}{\partial x}\right) - Q_{11} = 0 \tag{28a}$$

where

$$K_{11} = \int_0^b H_1 g_1^2\, dy \tag{28b}$$

$$K_{21} = \int_0^b H_2 g_{1,yyyy} g_1 dy \tag{28c}$$

$$K_{31} = \int_0^b H_3 g_{1,yy} g_1 dy \tag{28d}$$

$$K_{41} = \int_0^b H_8\, g_1^2 dy \tag{28e}$$

$$K_{51} = \int_0^b H_9 g_{1,yy} g_1 dy \tag{28f}$$

$$K_{61} = \int_0^b H_{10} g_{1,y} g_1 dy \tag{28g}$$

$$Q_{11} = \int_0^b q_0 g_1 dy \tag{28h}$$

For solving Eq. (28a), the mechanical boundary conditions (CCCC, SSSS, CSCS, CSSC) in terms of f(y) mentioned in figure 4 can be used as listed below:

$$\text{CCCC:} \qquad f(0) = 0, f(a) = 0, f_{,x}(0) = 0, f_{,x}(a) = 0 \tag{28i}$$

$$\text{SSSS:} \qquad f(0) = 0, f(a) = 0, f_{,xx}(0) = 0, f_{,xx}(a) = 0 \tag{28j}$$

$$\text{CSCS:} \qquad f(0) = 0, f(a) = 0, f_{,x}(0) = 0, f_{,x}(a) = 0 \tag{28k}$$

$$\text{CSSC:} \qquad f(0) = 0,\ f_{,x}(0) = 0, f(a) = 0, f_{,xx}(a) = 0 \tag{28l}$$

Here, CCCC represents fully clamped plate; SSSS represents fully simply supported plate; CSSC represents the plate with adjacent two edges clamped and remaining two edges simply supported; and CSCS represents plate with two opposite edges clamped and remaining two edges simply supported, whereas C denotes the clamped and S denotes the simply supported edge. In the present paper, we showed the utilization of the EKM only for CCCC and SSSS boundary, but this method can easily be extended to any arbitrary boundary conditions (Kumari and Shakya, 2017), just by changing Eqs. (28) and (30).

After solving Eq. (28), the obtained f(x) (let the solution is $f(x) = f_1(x)$) is introduced as priori known function for f(x) in the next step of EKM whereas g(y) is taken as an unknown function that needs to be solved. In the same way as before, we can derive ODE of g(y) after substituting updated $w_0 (= f_1 . g)$ in the weak form (Eq. 25).

$$\int_0^b \left[\int_0^a \left(H_1 g(y) \frac{\partial^4 f_1(x)}{\partial x^4} + H_2 f_1(x) \frac{\partial^4 g(y)}{\partial y^4} + H_3 \left(\frac{\partial^2 f_1(x)}{\partial x^2} \right) \left(\frac{\partial^2 g(y)}{\partial y^2} \right) - H_8\, g(y) \left(\frac{\partial^2 f_1(x)}{\partial x^2} \right) - H_9 f_1(x) \left(\frac{\partial^2 g(y)}{\partial y^2} \right) - H_{10} \left(\frac{\partial f_1(x)}{\partial x} \right) \left(\frac{\partial g(y)}{\partial y} \right) - q_0 \right) f_1(x) dx \right] \delta g(y) dy = 0 \tag{29}$$

From Eq. (29), the following ODE of g(y) is obtained.

$$K_{12}\, g + K_{22} \left(\frac{\partial^4 g}{\partial y^4} \right) + K_{32} \left(\frac{\partial^2 g}{\partial y^2} \right) - K_{42}\, g - K_{52} \left(\frac{\partial^2 g}{\partial y^2} \right) - K_{62} \left(\frac{\partial g}{\partial y} \right) - Q_{12} = 0 \tag{30a}$$

where

$$K_{12} = \int_0^a H_1 f_{1,xxxx} f_1 \, dx \tag{30b}$$

$$K_{22} = \int_0^a H_2 f_1^2 dx \tag{30c}$$

$$K_{32} = \int_0^a H_3 f_{1,xx} f_1 dx \tag{30d}$$

$$K_{42} = \int_0^a H_8 f_{1,xx} f_1 dx \tag{30e}$$

$$K_{52} = \int_0^a H_9 f_1^2 dx \tag{30f}$$

$$K_{62} = \int_0^a H_{10} f_{1,x} f_1 dx \tag{30g}$$

$$Q_{12} = \int_0^a q_0 f_1 dx \tag{30h}$$

For solving Eq. (30a), the requisite boundary conditions in terms of g(y) from the mechanical boundary conditions shown in figure 4 can be given as:

CCCC: $$g(0) = 0, g(b) = 0, g_{,y}(0) = 0, g_{,y}(b) = 0 \tag{30i}$$

SSSS: $$g(0) = 0, g(b) = 0, g_{,yy}(0) = 0, g_{,yy}(b) = 0 \tag{30j}$$

CSCS: $$g(0) = 0, g(b) = 0, g_{,yy}(0) = 0, g_{,yy}(b) = 0 \tag{30k}$$

CSSC: $$g(0) = 0, g_{,y}(0) = 0, g(b) = 0, g_{,yy}(b) = 0 \tag{30l}$$

After solving Eq. (30), the obtained g(y) (let the solution is $g(y) = g_1(y)$) from the aforementioned first iteration is then used as the priori function for g(y) in the next iteration step where f(x) is taken as an unknown function. Likewise, one can perform multiple iterations using the same solution technique based on Eq. (28) and (30) until the converged results, i.e., converged $w_0(x,y)$ is obtained. Generally, after two or three iterations, the solution gets converged.

2.5.2 Dynamic analysis based on Ritz method

In dynamic analysis, free vibration ($q_0 = 0$) of the present FGPM nanoplate incorporating both flexoelectricity and surface effect is performed using the Ritz method. In this section, in-plane vibration ($x - y$ plane) is neglected for the purpose of simplicity. The weak form of governing equation is derived from Eq. (17) and can be written as follows:

$$\int_{t_i}^{t_f}\int_0^a\int_0^b [\,(M_{xx}^* + N_{xxz})\delta\varepsilon_{xx}^1 + \left(M_{yy}^* + N_{yyz}\right)\delta\varepsilon_{yy}^1 + 2M_{xy}^*\delta\varepsilon_{xy}^1 + N_{xx}^* w_{0,x}\,\delta w_{0,x} + N_{yy}^* w_{0,y}\delta w_{0,y} + N_{xy}^*\,(w_{0,x}\,\delta w_{0,y} + w_{0,y}\,\delta w_{0,x}) + I_0\ddot{w}_0\,\delta w_0]\,dxdydt = 0 \tag{31}$$

After substituting the stiffness coefficients of Eq. (22) and strain-displacement relations (Eq. 16) into Eq. (31) and considering the time-dependent harmonic function of $w_0(x, y, t)$, the final equation of the weak form can be written as follows:

$$\int_0^a \int_0^b [D_1 W_{,xx} \delta W_{,xx} + D_1 W_{,yy} \delta W_{,yy} + D_3 W_{,yy} \delta W_{,xx} + D_4 W_{,xx} \delta W_{,yy} + D_5 W_{,xy} \delta W_{,xy}$$

$$+ D_{15} W_{,x} \delta W_{,x} + D_{16} W_{,y} \delta W_{,y} + D_{17} W_{,x} \delta W_{,y} + D_{18} W_{,y} \delta W_{,x} - I_0 \omega^2 W \delta W\,] dxdy = 0 \quad (32)$$

where ω is the frequency (Hz) of the FGPM nanoplate. The coefficients and their algebraic expressions are given in **Appendix B**. $W(x, y)$ is taken from harmonic (Euler) relation of the mid-plane displacement which is given as follows:

$$w_0(x, y, t) = W(x, y) e^{i\omega t} \quad (33)$$

The Ritz solution of the displacement W(x,y) for the square plate is assumed in the following form (Reddy, 2006):

$$W(x, y) = \sum_{i=1}^{M} \sum_{j=1}^{N} c_{ij} X_i(x) Y_j(y) \quad (34)$$

Selection of $X_i(x)$ and $Y_j(y)$ depend on the boundary conditions of the problem geometry. Further, M and N may be infinity (i.e., Eq. (34) signifying an infinite series). Hence, the standard approximate functions for X_i and Y_j for SSSS, CCCC, CSCS, SCSS etc. boundary conditions are chosen from the existing literature (Reddy, 2006) of plate theory (note that we have focused on CCCC and SSSS boundary conditions only for presenting numerical results).

CCCC:
$$X_i(x) = \left(\frac{x}{a}\right)^{i+1} - 2\left(\frac{x}{a}\right)^{i+2} + \left(\frac{x}{a}\right)^{i+3}$$
$$Y_j(y) = \left(\frac{y}{b}\right)^{j+1} - 2\left(\frac{y}{b}\right)^{j+2} + \left(\frac{y}{b}\right)^{j+3} \quad (35a)$$

SSSS:
$$X_i(x) = \left(\frac{x}{a}\right)^{i} - \left(\frac{x}{a}\right)^{i+1}$$
$$Y_j(y) = \left(\frac{y}{b}\right)^{j} - \left(\frac{y}{b}\right)^{j+1} \quad (35b)$$

CSCS:
$$X_i(x) = \left(\frac{x}{a}\right)^{i+1} - 2\left(\frac{x}{a}\right)^{i+2} + \left(\frac{x}{a}\right)^{i+3} \quad (35c)$$

$$Y_j(y) = \left(\frac{y}{b}\right)^j - \left(\frac{y}{b}\right)^{j+1}$$

SCSS (35d)

$$X_i(x) = \left(\frac{x}{a}\right)\left[1 - \left(\frac{x}{a}\right)\right]^{i+1}$$

$$Y_j(y) = \left(\frac{y}{b}\right)^j - \left(\frac{y}{b}\right)^{j+1}$$

Substituting Eqs. (35a) and (35b) in the weak form and by arranging the expression in the matrix form, the following equation is derived, from which the frequencies (ω) of the system can be calculated using different combinations of M and N.

$$([R]_{M\times N} - \omega^2 [B]_{M\times N})\{c\} = \{0\} \tag{36}$$

where

$$\begin{aligned} R_{(ij)(kl)} = \int_0^a \int_0^b [\, & D_1 X_{i,xx} Y_j X_{k,xx} Y_l + D_2 Y_{j,yy} X_i X_k Y_{l,yy} + D_3 X_i Y_{j,yy} X_{k,xx} Y_l + D_4 Y_j X_{i,xx} X_k Y_{l,yy} \\ & + D_5 X_{i,x} Y_{j,y} X_{k,x} Y_{l,y} + D_{15} X_{i,x} Y_j X_{k,x} Y_l + D_{16} X_i Y_{j,y} X_k Y_{l,y} + D_{17} X_{i,x} Y_j X_k Y_{l,y} \\ & + D_{18} X_i Y_{j,y} X_{k,x} Y_l \,]\, dxdy \end{aligned} \tag{37a}$$

$$B_{(ij)(kl)} = \int_0^a \int_0^b I_o X_i Y_j X_k Y_l \ dxdy \tag{37b}$$

For the sake of simplicity in formulation, we neglected the non-linear terms in the present study. In this context (regarding the non-linearity case), it is also possible to include nonlinear parameters within the computational framework. In other words, we can easily include geometric nonlinearity in the system and also nonlinearity in the Eqs. 25 and 32 for making the system more accurate. In that case, the solution will involve simultaneous nonlinear partial differential equations.

3. Numerical results and discussions

3.1 Validation and convergence studies

Before analyzing the numerical findings of the FGPM system, two different types of convergence and validation studies are needed to be performed to check the reliability of the results. In this investigation, two different approximate methods which are discussed in earlier section 2.5 are followed for studying the effects of flexoelectric and surface properties on an FGPM nanoplate. Among these, as the EKM approach is newly introduced here in the field of electromechanical analysis, to check the efficiency of this method for FGPM 2D-plate problems, the convergence study is carried out by comparing the deflection curve, i.e., transverse deflection along one edge ($x-$axis) of rectangular UD-FGPM nanoplates. Figure 5 shows that the convergence of the present iteration-based method is very rapid with a maximum of two or three iteration steps that are enough to get the converged results. Therefore, we have carried out a maximum of three iterations in the further analyses. As per the discussion in earlier sections, the initial guess function for $g_1(y)$ is needed to start the EKM method.

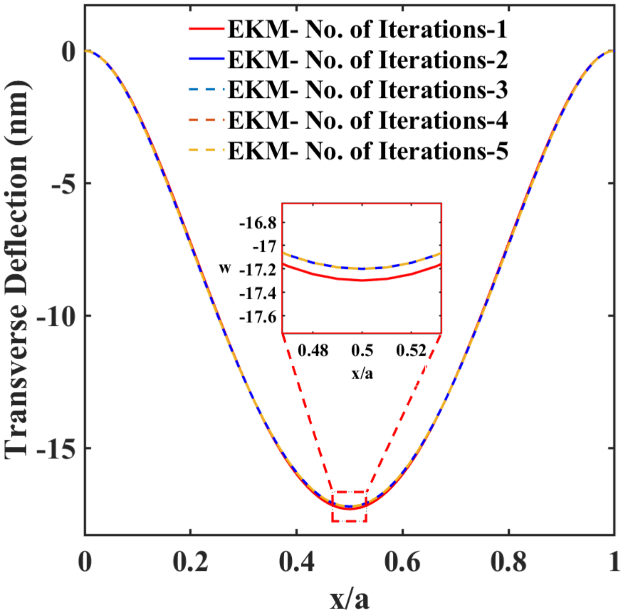

Fig. 5. Convergence plot for transverse deflection of UD-FGPM nanoplates with respect to aspect ratio considering function, $g_1(y) = y(y-b)$.

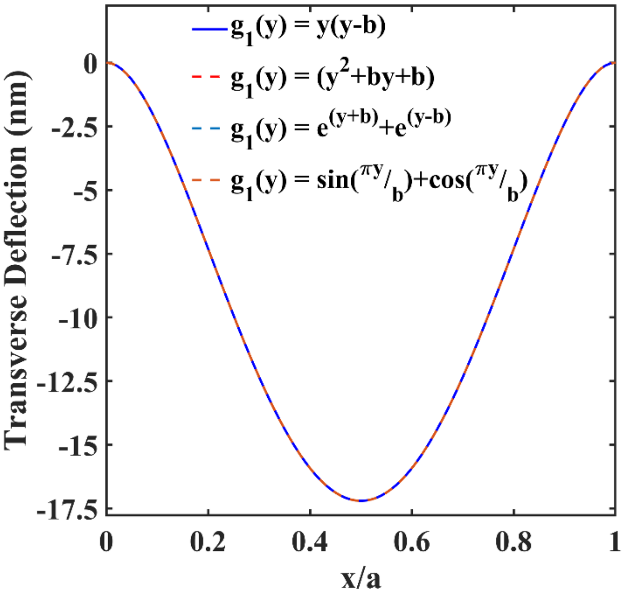

Fig. 6. Convergence plot for transverse deflection of UD-FGPM nanoplates with respect to aspect ratio considering three iterations.

In Fig. 6, the results are calculated using three different types of function – polynomial, exponential and trigonometric, wherein it can be concluded that the final result is unaffected by the initial guesses. We get almost the same center deflection from each initial choice. The magnitudes of the center deflections are shown in Table 1. From this, it is found that the maximum deflection is occurring at the center of the plate for each function and the difference between obtained values are in the order of $\sim 10^{-9}$ to $\sim 10^{-8}$ which strongly confirm the convergence efficiency of the present EKM approach. The above two conclusions are precisely matching with the discussions presented in the preceding sections as per Kerr and Alexander (1968). In the following subsections, the validation study is performed with respect to existing literature (Shingare and Naskar, 2021c; Yang et al., 2015) considering two illustrative cases for the static and dynamic analysis of flexo-surface FGPM nanoplates.

Table 1. Convergence study for transverse deflection of UD-FGPM nanoplates under three iterations.

Priori Function	Location of Max. deflection	Magnitude of Max. deflection (mm)
$g_1(y) = y(y - b)$	0.5	17.198756520806104
$g_1(y) = (y^2 + by + b)$	0.5	17.198756538984320
$g_1(y) = e^{y+b} + e^{y-b}$	0.5	17.198757361498956
$g_1(y) = \sin\left(\frac{\pi y}{b}\right) + \cos\left(\frac{\pi y}{b}\right)$	0.5	17.198756518719623

3.1.1 Case 1: Static and dynamic response of non-FGM flexoelectric nanoplates

We have first examined the static and dynamic responses of a non-FGM flexoelectric nanoplate from (Shingare and Naskar, 2021c) using the present model where we just neglect the surface effects (ξ_c and $\sigma_0 = 0$) on the upper and lower surface. This nanoplate is made of hybrid graphene reinforced piezoelectric composite (GRPC) material where all the edges are simply supported and a transverse load of 0.1MPa is acting upon it. Table 2 lists the material parameters and dimensions of the GRPC nanoplate used in this case study. For getting static and dynamic responses, Shingare and Naskar (2021c) used the Navier approach which we validate here for our present single-term extended Kantorovich method (EKM) and Ritz method, respectively. Figure 7 shows the static response of center deflection of hybrid GRPC nanoplate along the length whereas the dynamic response is shown by varying resonant frequency with plate aspect ratio in Fig. 8. From figures 7 and 8, it can be observed that the results obtained from EKM and Ritz solutions are found to be in excellent agreement with the results estimated by Shingare and Naskar (2021c). Concerning the issue of non-linearity mentioned in previous Section 2.5.1, these figures also clearly indicate that the effect of neglecting non-linear terms is acceptable even in flexoelectric cases ($f_{14} \neq 0$).

Table 2. Material properties and dimensions of hybrid GRPC nanoplates.

Plate thickness, h	20 nm
Plate aspect ratio, a/h	45
c_{11}	112.43 GPa
c_{12}	3.34 GPa
c_{66}	2.03 GPa
e_{31}	-6.9337 C/m^2
μ_{33}	3.264×10^{-9} C/V. m
f_{14}	1×10^{-7} C/m

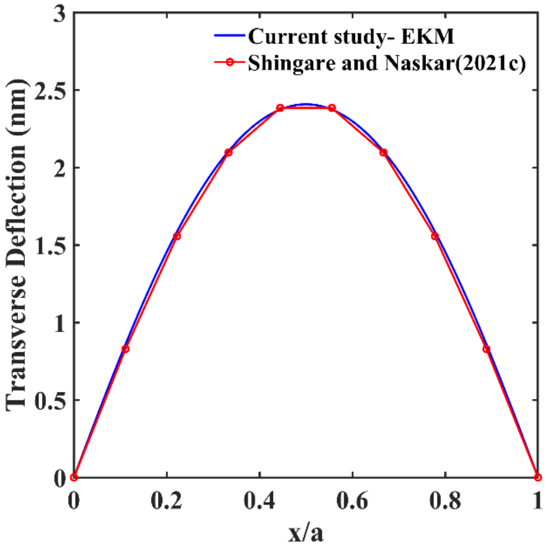

Fig. 7. Comparison of two different models for the static transverse deflection of nanoplates along the length.

3.1.2 Case 2: Static and electric potential response of non-FGM nanoplates considering surface effects

Here, we have examined and validated the surface effect of a 2D non-FGM nanoplate. As our problem statement is on open-circuit condition and due to lack of literature on open-circuit, we validate our results indirectly with Yan and Jiang (2012a) which is based on closed-circuit conditions. This validation is based on one simple observation of the internal electric field in both cases. If we compare Eq. (14) with the electric field

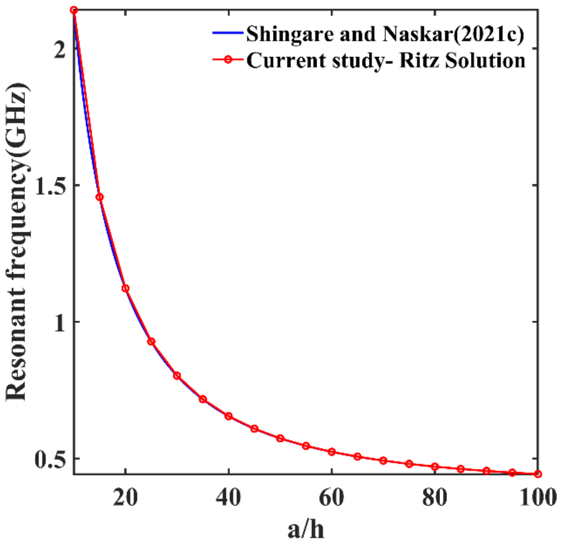

Fig. 8. Comparison of two different models for the resonant frequency of nanoplates in terms of aspect ratio.

Table 3. Material and surface parameters of 2D non-FGM plates.

Plate aspect ratio, a/h	30
Material	PZT-5H
c_{11}	126 GPa
c_{12}	55 GPa
c_{66}	2.03 GPa
e_{31}	-6.5 C/m^2
e_{33}	23.3 C/m^2
μ_{33}	1.30×10^{-8} C/V. m
f_{14}	0 C/m
c_{11}^s	7.56 N/m
e_{31}^s	-3.0 $\times 10^{-8}$ C/m
σ_0	1.0 N/m

the internal electric field (E_z) is the same. We have also validated the aforementioned statement by plotting the electric potential distribution on the upper and lower layer of nanoplate in figures 9 and 10 from our analytical model considering two instances (UD and LD distributions) and observed that potential is zero on the upper

(E_z) equation mentioned by Yan and Jiang (2012a), we can conclude that non-flexo ($f_{14} = 0$) open-circuit case is equivalent to zero voltage ($V = 0$) close-circuit case for the present nanoplate problem because in both cases surface (≈ 0 V) and the lower surface is equivalent to a ground node. The material properties and surface parameters used in this case are enlisted in Table 3.

In figure 11, it can be observed that there is a dependency of plate thickness on its deflection in the presence of positive residual surface stress ($\sigma_0 = 1\ \mathrm{N/m}$) and with the increase of thickness, the effect of surface stress diminishes. From figure 11, it can also be concluded that the results obtained using the EKM solution are found in good agreement with the results estimated by Yan and Jiang (2012a). Now if we include flexoelectric property ($f_{14} \neq 0$) in our present analytical model along with surface effects, there will be the inclusion of some non-zero potential in upper surfaces and it is observed that the value of this potential (V) is very less (nearly zero), but it is more than the previous non-flexo cases. Figure 12 shows the potential distribution of flexo-surface FGPM nanoplates considering UD and LD cases. The same trend is also observed in the case of a flexoelectric GNC nanowire (Kundalwal et al., 2020).

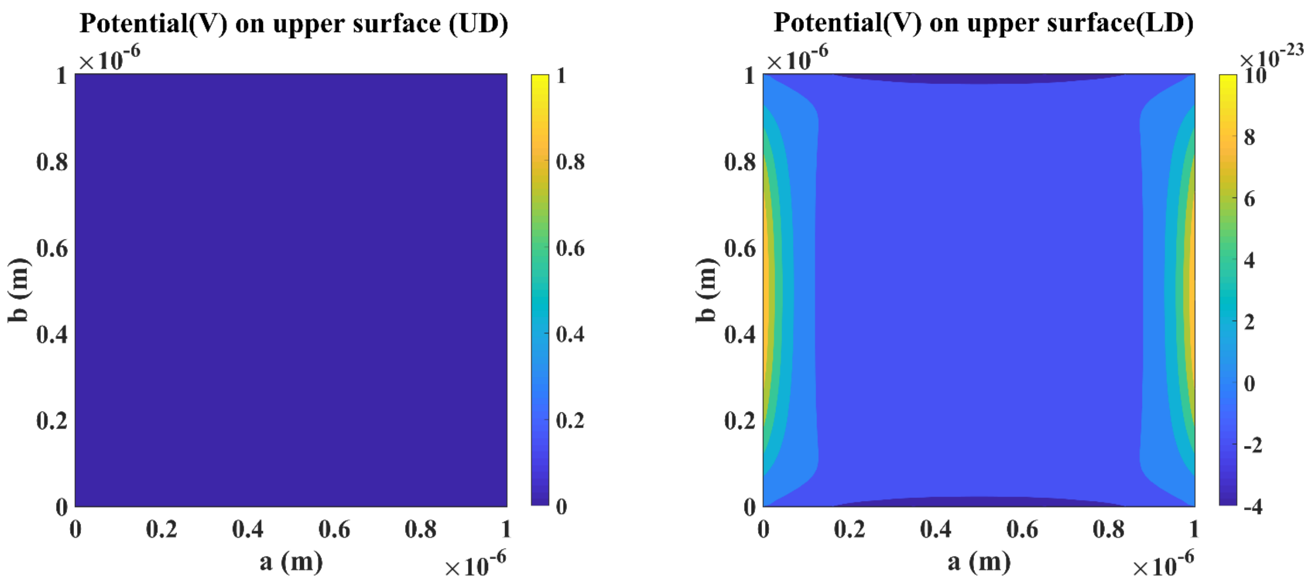

(a) (b)

Fig. 9. Electric potential distribution on upper surface of nanoplates considering: **(a)** UD and **(b)** LD.

3.2 Static response of FGPM nanoplates

The classical thin plate theory is adopted in this investigation by neglecting nonlinear terms to determine the electromechanical response (static, dynamic, and electrical behavior) of the FGPM nanoplate. The FGPM nanoplate is initially subjected to a uniformly distributed load $q_0 = 0.05\ \mathrm{pN/nm^2}$. Even though substantial advances are reported over the past couple of decades, still various complexities exist related to the flexoelectric coefficient (f_{14}) for PVDF based structures. Several authors have stated that the range of its magnitude typically varies in between 10^{-10} to 10^{-5} $\mathrm{C/m}$ (Baskaran et al., 2011; Zhou et al., 2017). The material properties of GPLs and PVDF and related dimensional parameters are summarized in Table 4. Here,

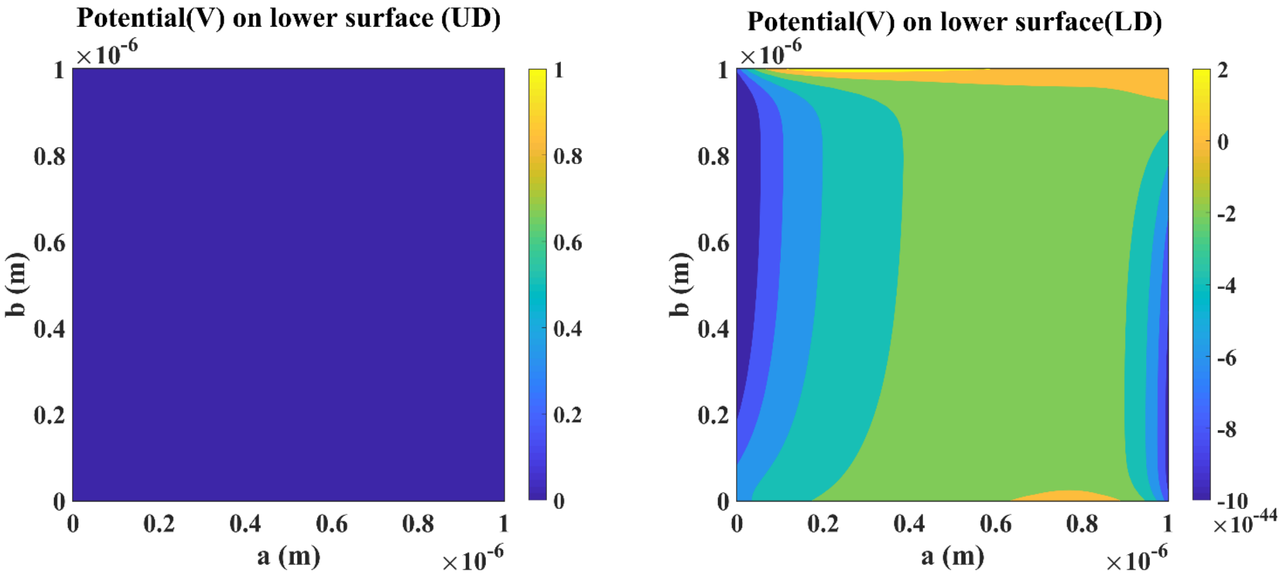

(a) (b)

Fig. 10. Electric potential distribution on lower surface of nanoplates considering: **(a)** UD and **(b)** LD.

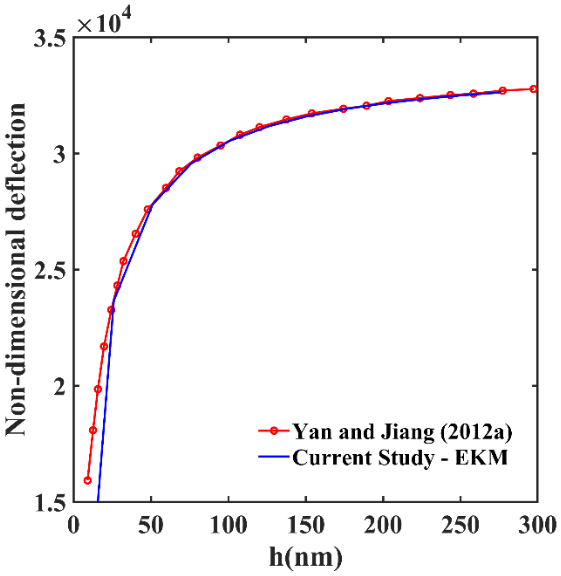

Fig. 11. Variation of non-dimensional deflection of nanoplates with respect to thickness.

for sake of simplicity, we have adopted the cubic crystal symmetry for graphene reinforced polymer matrix composites. The different influencing parameters on the static deflection of nanoplates are investigated and discussed here in two sections, i.e., considering only flexoelectric effect and considering both surface and flexoelectric effects. In later sections, we have also pointed out few limitations of our present model in predicting its electromechanical characteristics.

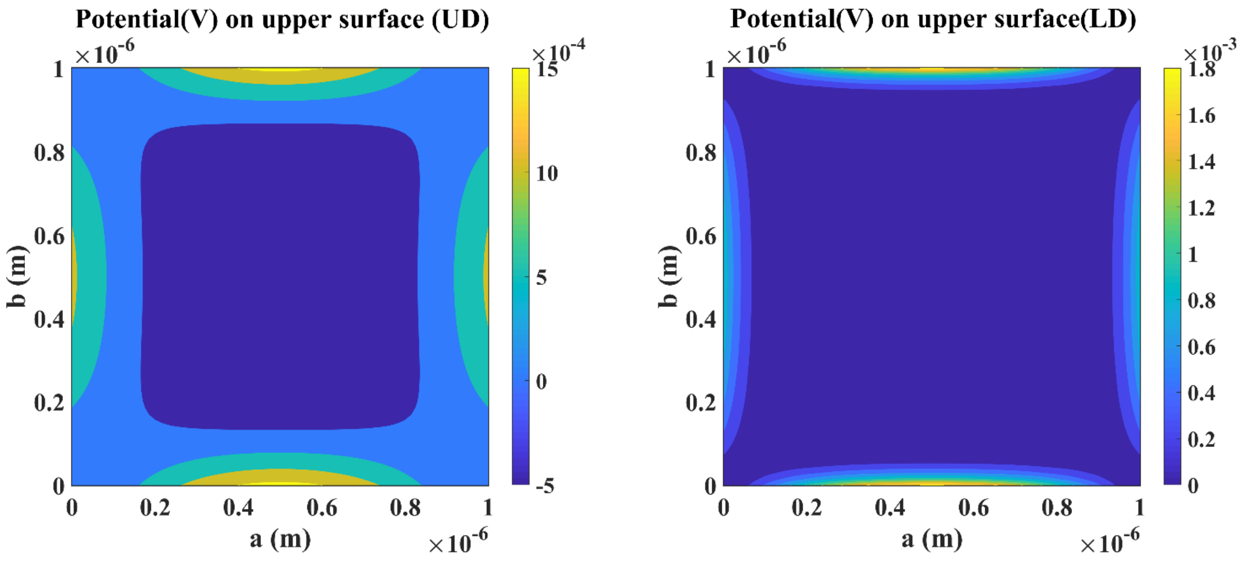

(a) (b)

Fig. 12. Electric potential distribution on the upper surface of flexo-surface nanoplates considering: **(a)** UD and **(b)** LD.

3.2.1 Consideration of only flexoelectric effect (ξ_c and $\sigma_0 = 0$)

In this section, we investigated the effect of various parameters such as plate thickness (h), aspect ratio (a/h), in-plane dimensions (a or b), etc., considering the center deflection and deflection ratio (r_{flex} and r_{sur}) as our reference. The deflection ratio is given by:

$$r_{flex} = \frac{\text{Deflection considering flexoelectric effect}}{\text{Deflection without flexoelectric effect}}$$

Figure 13 shows the effects of thicknesses on a square FGPM nanoplate's deflection ratio with three different distributions for CCCC boundary condition. Here the width-to-thickness ratio of nanoplate is kept constant, i.e., $a/h = 50$. It can be observed, with the increase of thickness, the deflection ratio tends to unity which indicates that the flexoelectric effect is more pronounced in case of a lesser thickness of the plate. From this, it can be concluded that the phenomenon of flexoelectricity is size-dependent. In addition, the flexoelectric FGPM nanoplates with LD and UD distribution show almost the same behaviour while in the case of PD, we observe less flexoelectric effect than UD and LD because it achieves the saturation stage ($r_{flex} = 1$) faster. In all three distributions, pure flexoelectricity stiffens the FGPM plate in terms of maximum static deflection.

The effects of thickness and in-plane dimensions of the nanoplate on its static bending response are now investigated in the following figures. In figure 14, we have kept in-plane dimensions (a and b) constant

Table 4. Geometric and material properties of constituents of FGPM (Arefi et al., 2018; Z. Zhao et al., 2020).

Elastic and geometrical properties		**Piezoelectric constants** $(\mathrm{C/m^2})$	
$\mathrm{W_{char}}$	1%	$\mathrm{e_{31}^{PVDF}}$	50.535×10^{-3}
$\mathrm{l_{GPL}}$	3 nm	$\mathrm{e_{32}^{PVDF}}$	13.212×10^{-3}
$\mathrm{w_{GPL}}$	1.8 nm	**Surface parameters**	
$\mathrm{t_{GPL}}$	0.7 nm	Charac. length (ξ_c)	1 nm
α	100×1000	σ_0	1 or 0 $\mathrm{N/m}$
ρ_{GPL}	$1060\ \mathrm{kg/m^3}$	σ_{xy}^{0}	$0\ \mathrm{N/m}$
ρ_{PVDF}	$1920\ \mathrm{kg/m^3}$	**Dielectric constants** $(\mathrm{F/m})$	
$\mathrm{E_{GPL}}$	1010 GPa	a_{33}^{PVDF}	0.59571×10^{-9}
$\mathrm{E_{PVDF}}$	1.44 GPa	**Flexoelectric parameters**	
ν_{GPL}	0.186	$\mathrm{f_{3113}}$	$\approx 1 \times 10^{-7}\ \mathrm{C/m}$
ν_{PVDF}	0.29	$\mathrm{f_{3223}}$	$\approx 1 \times 10^{-7}\ \mathrm{C/m}$

whereas, in figure 15, the thickness (h) is kept constant. Figure 14 illustrates that all distributions have a stronger flexoelectric impact if the aspect ratio is large, i.e., when the thickness is small. Here, the deflection ratios of UD and LD both drop to 0.56, whereas PD only drops to 0.69 for aspect ratio, $a/h = 100$.

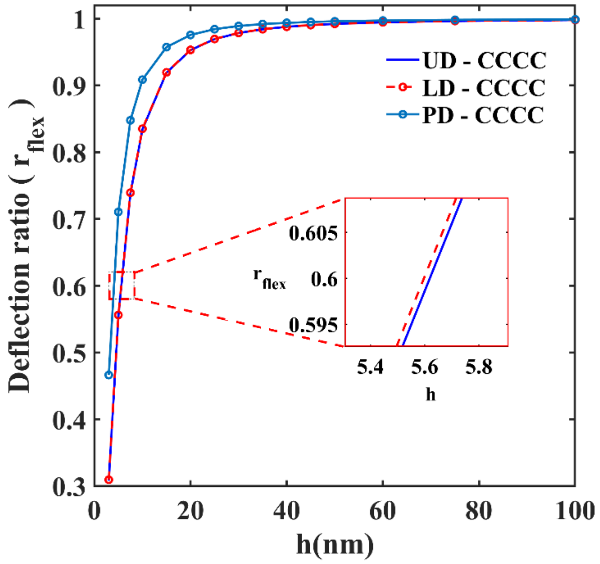

Fig. 13. Effect of thickness (h) on deflection ratio $(\mathrm{r_{flex}})$ of flexo FGPM nanoplates at constant aspect ratio $(\mathrm{a = b = 50h})$.

Figure 15 shows another important aspect of size-dependency of flexoelectric property. When the thickness is kept constant, in-plane dimensions have nearly no effect on the deflection ratio for that particular range of aspect ratios (10 to 100). In this case, we observe the deflection ratio of PD is more than UD. For the sake of brevity, we have not presented the results for LD nanoplates as it shows similar behavior as that of UD nanoplate. The reason for such thickness dependency is that the strain gradient has an inverse relationship with the material dimension i.e., size of structures (Kumar et al., 2018) while it has a direct effect on flexoelectricity (Kundalwal, et al., 2020). This is also the reason why we get more flexoelectric properties in the case of UD. We also observed from our analytical model that the strain gradient is more in the case of UD or LD as compared to PD-FGPM nanoplate. For example, the values of strain gradient ($\varepsilon_{xx,z}$) at centre in UD and PD for a square flexoelectric nanoplate ($f_{14} = 10^{-7}\ \mathrm{C/m}$) with $h = 20\ \mathrm{nm}, a = b = 50h$ are $2.476 \times 10^{5}\ \mathrm{m}^{-1}$ and $1.913 \times 10^{5}\ \mathrm{m}^{-1}$, respectively.

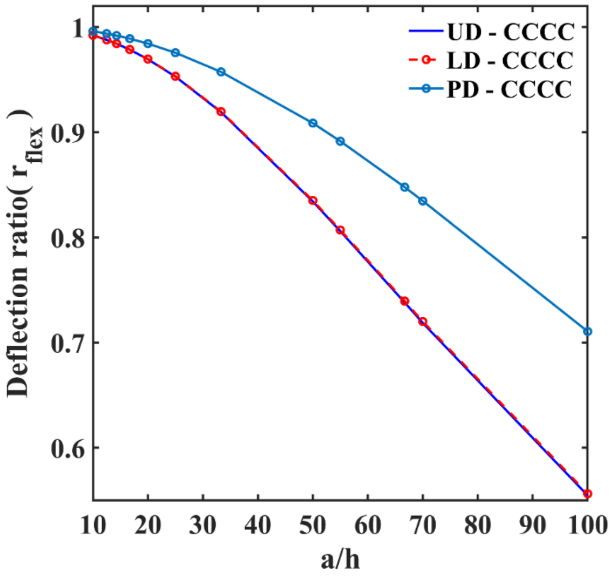

Fig. 14. Effect of aspect ratios (a/h) on the deflection ratio (r_{flex}) of flexo FGPM plates at constant in-plane dimension ($a = b = 500\ \mathrm{nm}$).

Figure 16 represents the maximum transverse deflections of UD- and PD-FGPM nanoplates with and without consideration of flexoelectricity. Here, we have used a plate thickness of $h = 20\ \mathrm{nm}$ to study the flexoelectric effect on the static bending deflection because both distributions don't reach saturation at $h = 20\ \mathrm{nm}$ as shown in figure 13. The difference in transverse deflection due to the flexoelectric effect is maximum near the center of UD-FGPM nanoplates and is less for PD case which also validates the observations of figures 13, 14 and 15. From figure 16 (a), it can be concluded that PD-FGPM flexoelectric plate shows stiffer behavior than the UD-FGPM plate, which is also in agreement with existing literature (Z. Zhao et al., 2020). Like conventional FGM plates (Talha and Singh, 2010), figure 16 (b) also shows the center deflection of the SSSS flexoelectric plate is more than the CCCC plate as the bending stiffness of the CCCC plate is higher. It is also observed, due to consideration of the flexoelectric effect there is a significant reduction in deflection of FGPM nanoplates.

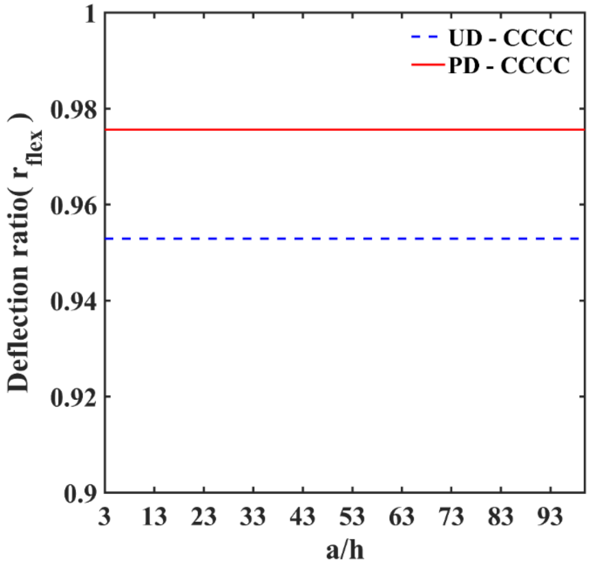

Fig. 15. Effect of aspect ratios (a/h) on the deflection ratio (r_{flex}) of flexo FGPM plates at a constant thickness $(h = 20\ nm)$. The results corresponding to LD nanoplates are similar to that of the UD case.

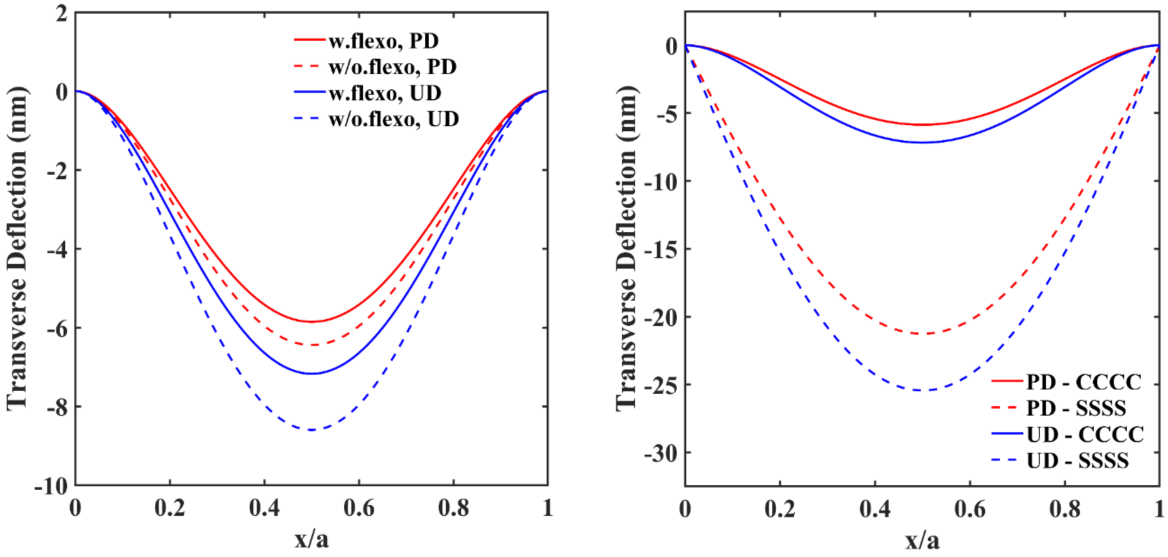

(a) (b)

Fig. 16. Variation of transverse deflection of flexo FGPM nanoplates along longitudinal axis (x) with different distribution of GPLs. **(a)** the effect of flexoelectric effect over non-flexoelectric effect **(b)** SSSS and CCCC boundary conditions. The results corresponding to LD nanoplates are similar to that of the UD case in both cases.

Figure 17 shows the variation of transverse deflection of the clamped-clamped FGPM nanoplate considering different distribution and flexoelectric coefficients ranging from $10^{-10}\ \mathrm{C/m}$ to $10^{-6}\ \mathrm{C/m}$. It is evident that the effect of flexoelectricity significantly affects the overall static deflections of the FGPM nanoplate. The deflection continues to decrease as the flexoelectric coefficient increases in magnitude. We observe the same trend of results in published literature (Shingare and Naskar, 2021c) which affirms the validity of our present model (EKM) further. In addition to this, in all three distributions, there exists a significant reduction in the magnitude of deflection in between $\mathrm{f}_{14} = 10^{-6}\ \mathrm{C/m}$ and $\mathrm{f}_{14} = 10^{-8}\ \mathrm{C/m}$ whereas after $\mathrm{f}_{14} = 10^{-8}\ \mathrm{C/m}$, this reduction is almost negligible. From the observations of figures 16 (a) and 17, one can report another prominent conclusion that as flexoelectric coefficient increases there is a significant reduction in the static deflection (figure 17), while there will be one case where there will be no effect of flexoelectricity, i.e., deflection with and without flexoelectric effect will be same for all aspect ratios. In that case, the deflection ratio, $\mathrm{r}_{\mathrm{flex}} \approx 1$. The same trend of results was also observed in the existing literature (Shingare and Kundalwal, 2019) on the non-FGM graphene/polyimide nanocomposite structures.

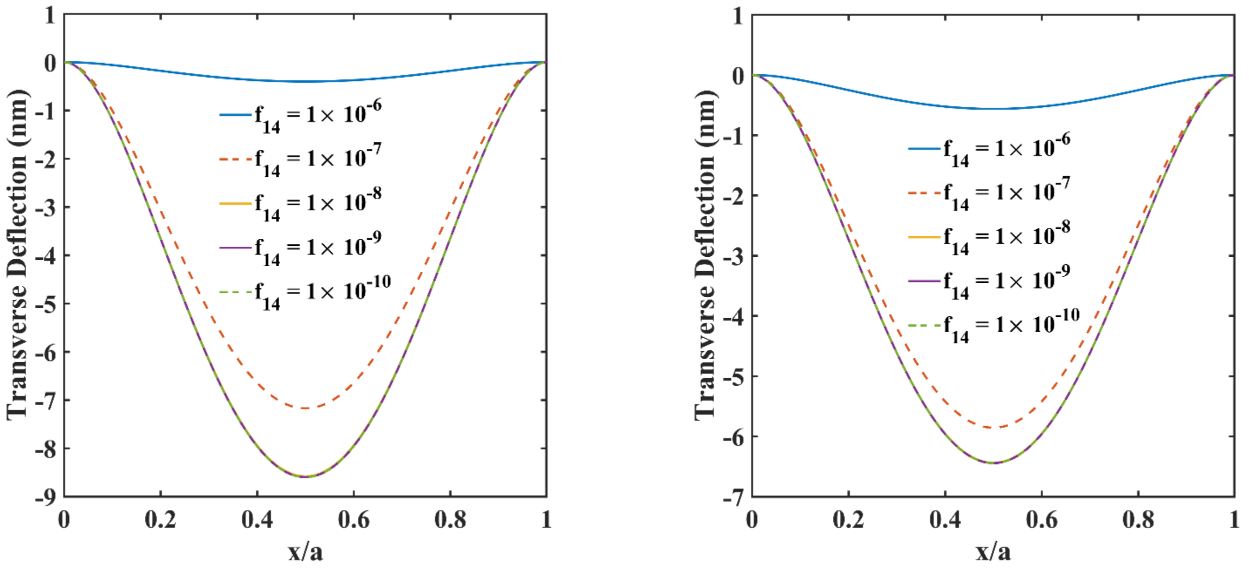

(a) (b)

Fig. 17. Variation of transverse deflection of flexo FGPM nanoplates for various flexoelectric coefficients and distributions: **(a)** UD and **(b)** PD. The results corresponding to LD nanoplates are similar to that of the UD case.

Figures 18 and 19 illustrate the effect of two influencing parameters, the total weight fraction of GPLs ($\mathrm{W}_{\mathrm{GPL}}^{\mathrm{t}}$) in the PVDF matrix and piezoelectric multiple (α), on the static bending deflection of a square flexoelectric nanoplate. Due to the incorporation of more GPLs into the FGPM system or due to an increase in the theoretical value of piezoelectric multiple (α), there is an increase in the overall stiffness of composite which directly influences the bending rigidity of nanoplates. This is one of the reasons for the decrement of static deflection with an increment of GPLs weight fraction and piezoelectric multiple. After analyzing figures 17, 18 and 19, it is evident that the deflection ratio or effect of flexoelectricity on static deflection not only depends on size parameters of the structure but also on the value of its flexoelectric coefficient, GPLs weight fraction and piezoelectric multiple.

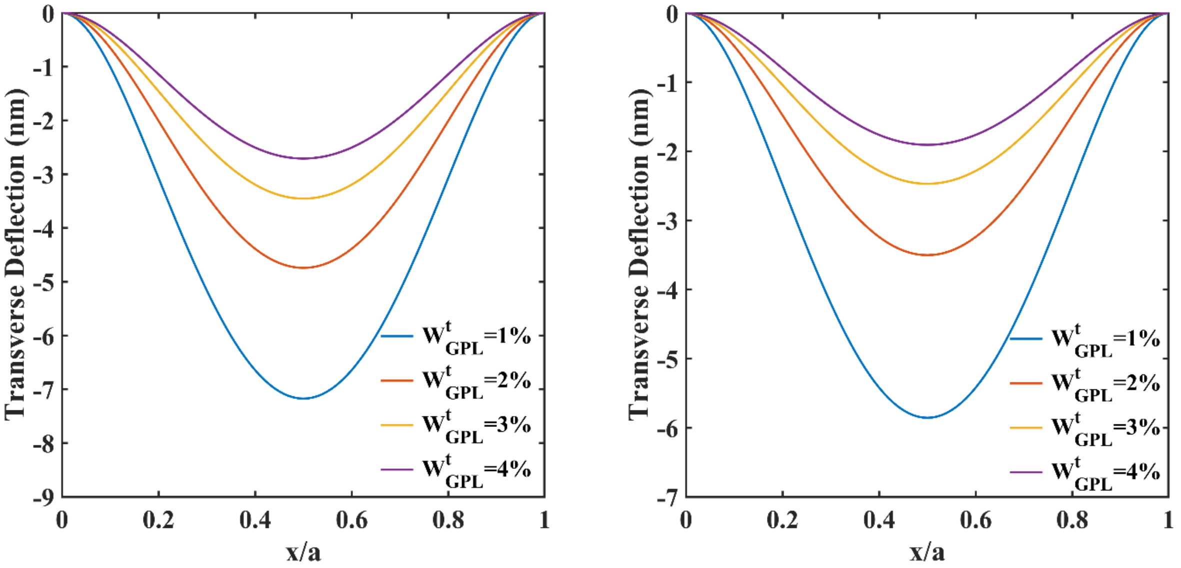

(a) (b)

Fig. 18. Variation of transverse deflection of flexo FGPM nanoplates for different weight fractions of GPLs and distributions: **(a)** UD and **(b)** PD. The results corresponding to LD nanoplates are similar to that of the UD case.

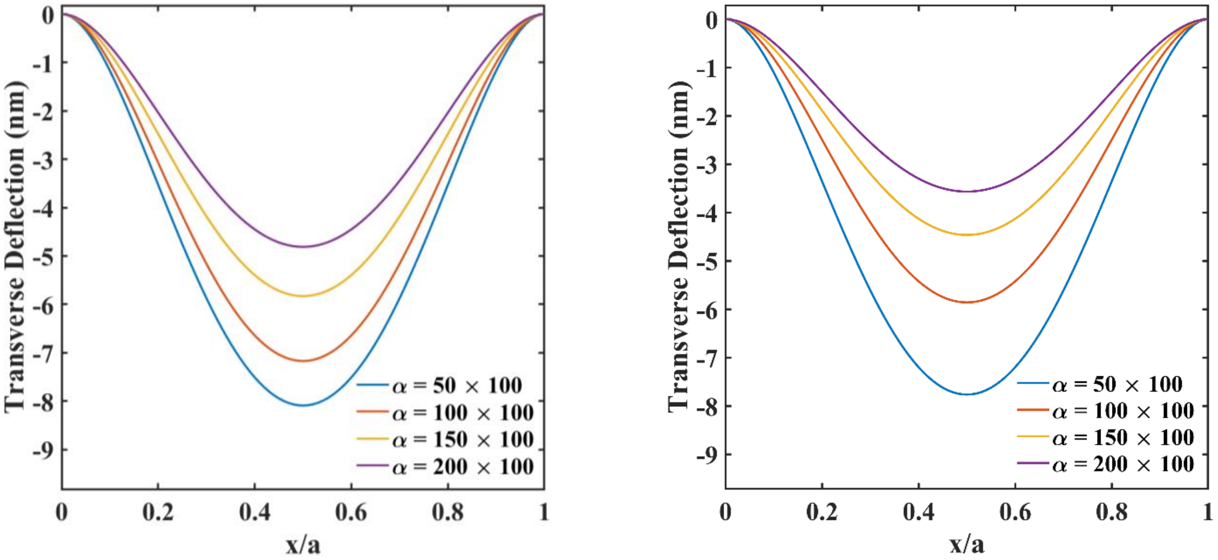

(a) **(b)**

Fig. 19. Variation of transverse deflection of flexo FGPM nanoplates for various piezoelectric multiples and distributions: **(a)** UD and **(b)** PD. The results corresponding to LD nanoplates are similar to that of the UD case.

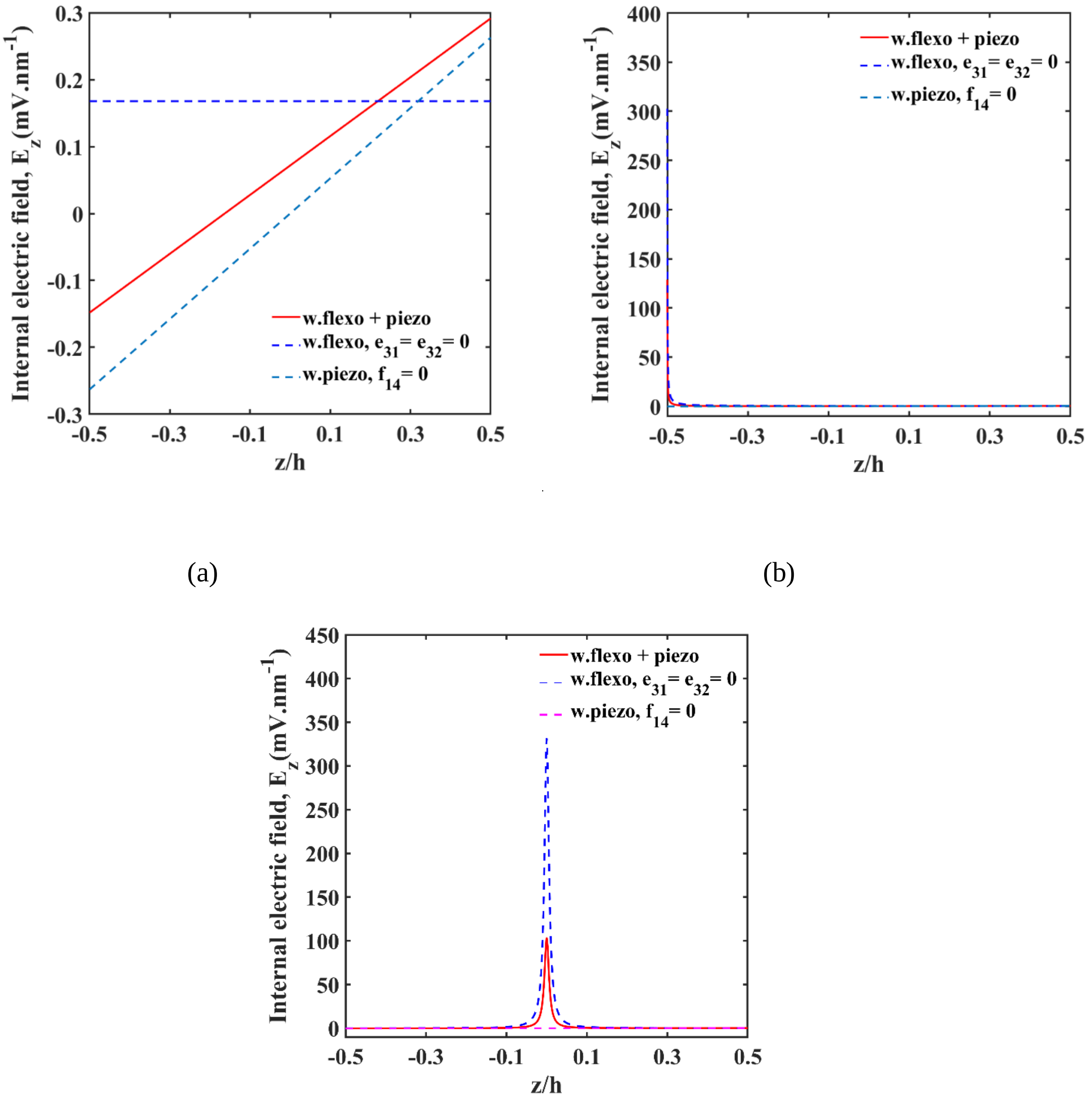

(a)

(b)

(c)

Fig. 20. Electric field variation along thickness of FGPM nanoplates for various distributions: **(a)** UD, **(b)** LD and **(c)** PD.

Figure 20 depicts the distribution of internally generated electric field (E_z) along the thickness of CCCC flexoelectric nanoplate for three different distributions. As per the discussion in section 2.3, there will be contributions of both flexoelectricity and piezoelectricity in the induced electric field of the open-circuit case. The results associated with electric filed considering piezoelectricity, flexoelectricity, and both piezoelectricity and flexoelectricity are illustrated in Fig. 20 (a, b and c). In the case of UD-FGPM, a linear variation of the electric field is observed whereas in LD- and PD-FGPM, a linear variation is observed except end and center position, respectively. Such a linear variation in case of UD-FGPM is in coherence with the observations of

Yan and Jiang (2012b). In case of LD- and PD-FGPM, there exists a jump in the field at the end and middle position, respectively, and the magnitude of LD or PD field is more than that of the UD case.

3.2.2 Consideration of flexoelectric and surface effects ($\boldsymbol{\xi_c}$ and $\boldsymbol{\sigma_0 \neq 0}$)

Along with flexoelectricity, the surface effect is one of the important influencing factors in predicting the electromechanical behavior of nanoplates. In this analysis, we also considered the deflection ratio ($\mathrm{r_{sur}}$) and center deflection as our reference. The deflection ratio by considering surface effect can be given as:

$$\mathrm{r_{sur}} = \frac{\text{Deflection considering flexoelectric and surface effect}}{\text{Deflection without flexoelectric and surface effect}}$$

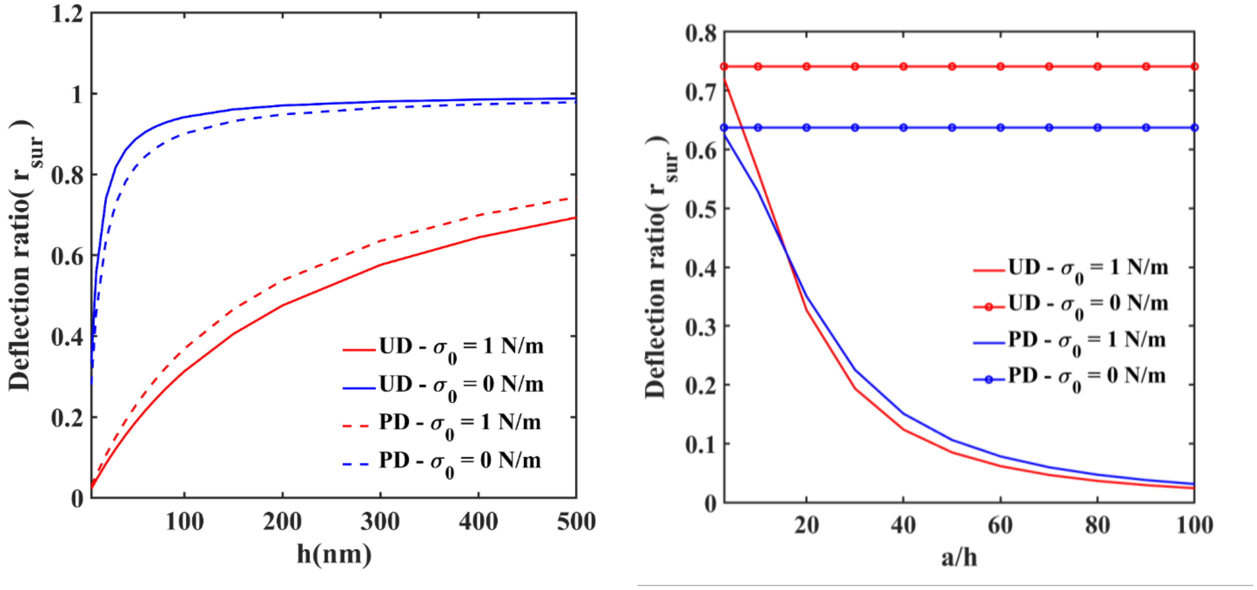

(a) (b)

Fig. 21. (a) Effect of thickness (h) on deflection ratio ($\mathrm{r_{sur}}$) of flexo-surface FGPM nanoplates at constant aspect ratio ($\mathrm{a = b = 50h}$) and **(b)** Effect of aspect ratios ($\mathrm{a/h}$) on deflection ratio ($\mathrm{r_{sur}}$) of flexo-surface FGPM nanoplates for thickness ($\mathrm{h = 20\ nm}$). The results corresponding to LD nanoplates are similar to that of the UD case in both cases.

In the static deflection of a plate, the sign of the surface residual stress (σ_0) is crucial. In case of negative residual stresses, the mechanical buckling instability occurs at a certain range of thickness for the applied transverse load ($\mathrm{q_0}$) and thus, it results in large deformation. As in this paper, the discussion is being limited to the static deflection and dynamic behavior of nanoplates, we consider only non-negative residual surface stresses ($\sigma_0 = 1$ and 0) in further analyses to avoid buckling.

Figures 21 (a and b) demonstrate the resultant effect of flexoelectricity and surface residual stress on the static bending deflection of square flexo-surface FGPM nanoplate against its thickness and aspect ratio, respectively. In figure 21(a), we kept the aspect ratio ($\mathrm{a/h = 50}$) whereas, in figure 21(b), the thickness is kept constant ($h = 20$ nm). In all these combinations, one can observe that the deflection ratio is less than 1 which indicates that this combined effect stiffens the FGPM nanoplate. From our analysis, it can be observed that the percentage reduction of deflection is more when we incorporate the surface effect. For example, for a square UD-FGPM nanoplate $(\mathrm{h} = 20\ \mathrm{nm};\ \mathrm{a/h} = 50)$, pure flexoelectricity reduces the static deflection of the conventional piezoelectric nanoplate by 4.71% whereas the combined effect of surface and flexoelectricity reduces it by 26 % – 91.5 % depending upon the sign and magnitude of residual surface stresses. In figure 21(a), with the reduction of surface residual stresses $(1 \text{ to } 0\ \mathrm{N/m})$, the combined effect also diminishes. Unlike pure flexoelectricity (refer to figure 13), when residual surface stress is zero, the deflection ratios of PD- and UD- FGPM are inverted, i.e., $\mathrm{UD} > \mathrm{PD}$.

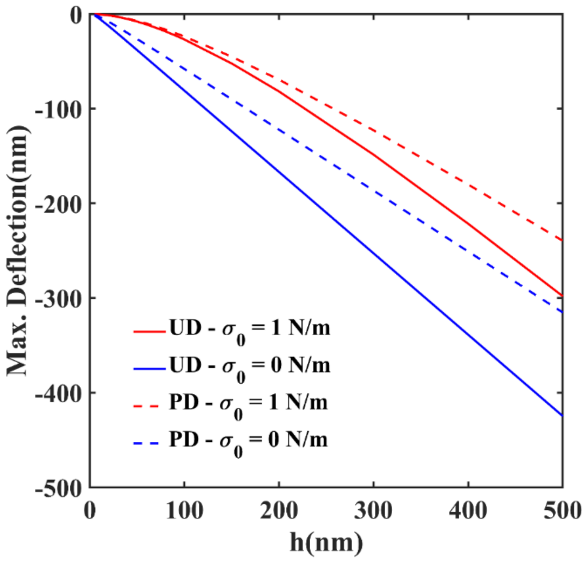

Fig. 22. Variation of maximum deflection of flexo-surface FGPM nanoplates against the thickness (h) $(\mathrm{a} = \mathrm{b} = 50\mathrm{h})$. The results corresponding to LD nanoplates are similar to that of the UD case.

In figure 21(b), it can be observed, for zero residual stress, the deflection ratio is almost independent of in-plane dimensions if the thickness is fixed, which is similar to the pure flexoelectricity case. But when the residual surface stress is non-zero, there is a reduction in $\mathrm{r}_{\mathrm{sur}}$ and it becomes dependent on in-plane dimensions. It can be also seen that there exists one critical aspect ratio $(\mathrm{a/h} = 15.8)$ where PD and UD give the same value of $\mathrm{r}_{\mathrm{sur}}$ and after that, we get $\mathrm{r}_{\mathrm{sur}}(\mathrm{PD}) > \mathrm{r}_{\mathrm{sur}}(\mathrm{UD})$. Surface effects become increasingly apparent in all distributions as in-plane dimensions increase. Figure 22 represents the maximum (center) deflection of flexo-surface FGPM nanoplate with respect to its thickness for UD and PD distribution with and without considering residual surface stress $(\sigma_0 = 1 \text{ and } 0)$. It can be seen that the effect of surface and flexoelectricity decreases as there is an increment in the thickness of flexo-surface nanoplate, and for both the residual surface stresses, the deflection is less for PD which is similar to the previously discussed pure flexoelectricity case.

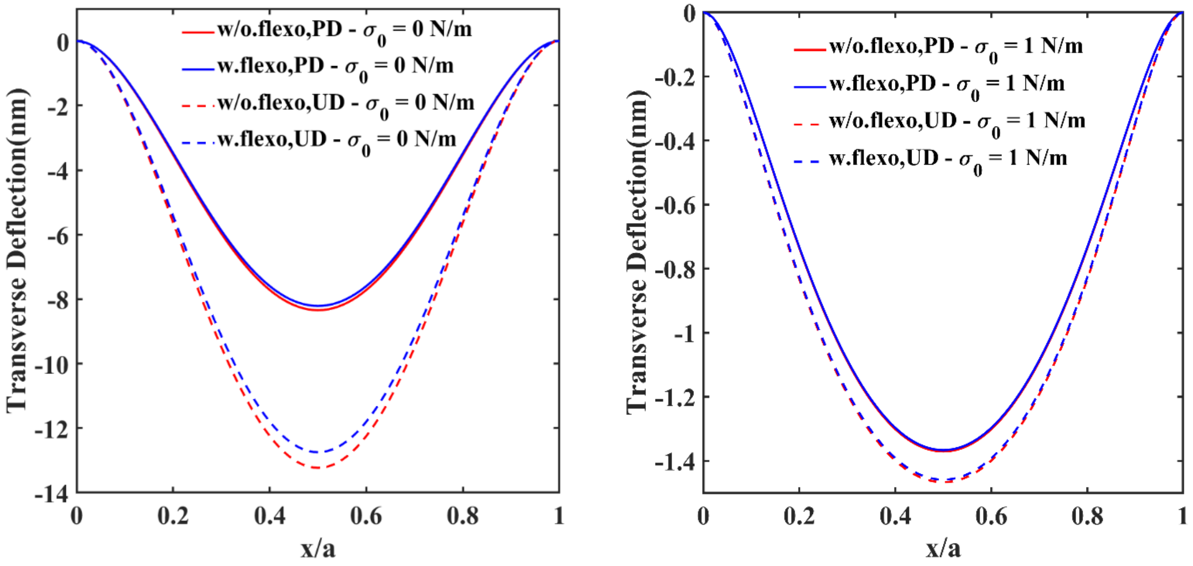

(a) (b)

Fig. 23. Variation of transverse deflection of flexo-surface FGPM nanoplates along the longitudinal axis (x) for LD and UD distribution with surface effects: **(a)** $\sigma_0 = 0$ and **(b)** $\sigma_0 = 1$ N/m. ($\mathrm{h} = 20$ nm, $\mathrm{a} = \mathrm{b} = 50\mathrm{h}$). The results corresponding to LD nanoplates are similar to that of the UD case.

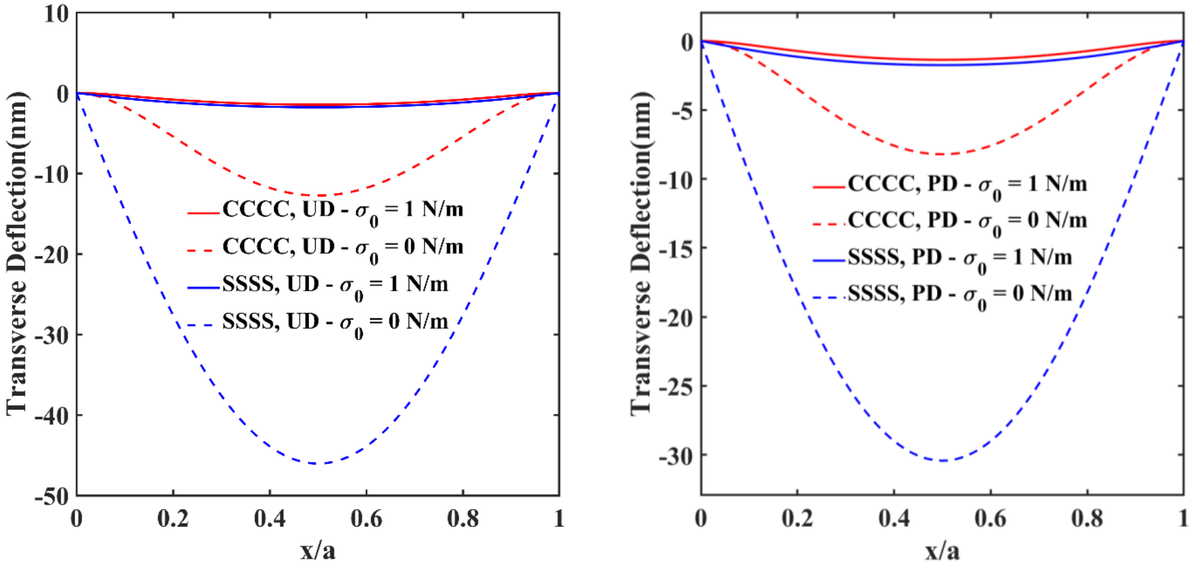

(a) (b)

Fig. 24. Variation of transverse deflection of CCCC and SSSS flexo-surface FGPM nanoplates along longitudinal axis (x) with different distributions: **(a)** UD and **(b)** PD. ($\mathrm{h} = 20$ nm, $\mathrm{a} = \mathrm{b} = 50\mathrm{h}$). The results corresponding to LD nanoplates are similar to that of the UD case.

Figure 23 investigates the effect of surface and flexoelectricity on flexo-surface FGPM nanoplate with thickness and in-plane dimension as $\mathrm{h} = 20$ nm and $\mathrm{a} = \mathrm{b} = 50\mathrm{h}$, respectively. As per the discussion in figure 22, it can be seen that PD-FGPM shows less deflection than UD-FGPM. Here, the effect of flexoelectricity reduces when we increase the residual stress from 0 to 1 N/m. In figure 23(a) ($\sigma_0 = 0$), the difference in static

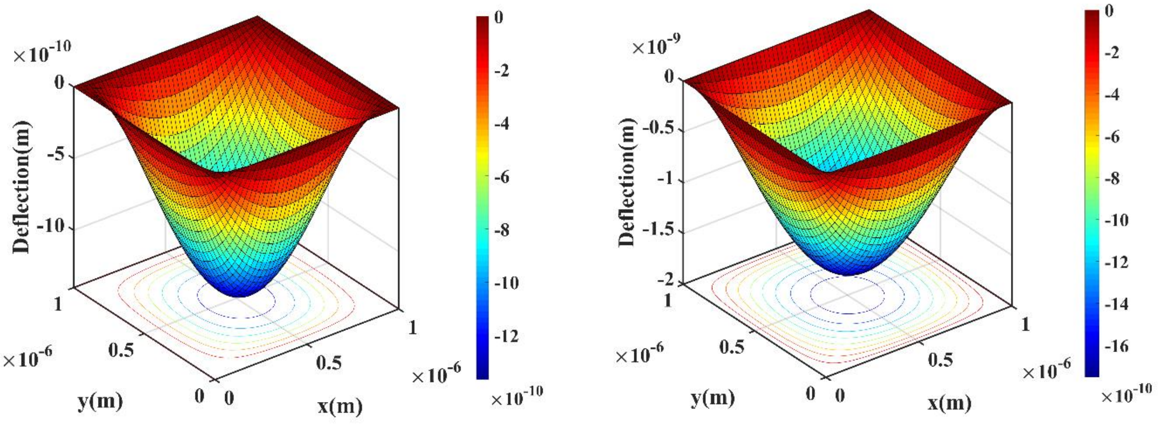

(a) (b)

Fig. 25. 3D representation of deflection of flexo-surface FGPM nanoplates with different boundary conditions: **(a)** CCCC and **(b)** SSSS. $(\mathrm{h} = 20\ \mathrm{nm}, \mathrm{a} = \mathrm{b} = 50\mathrm{h}, \sigma_0 = 1)$.

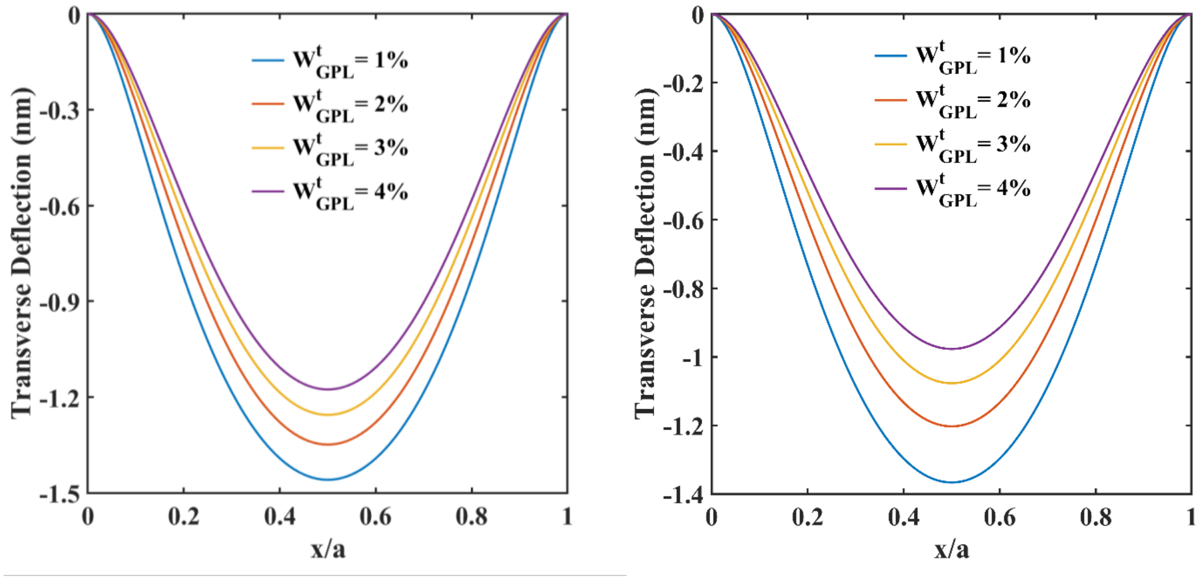

(a) (b)

Fig. 26. Variation of transverse deflection of flexo-surface FGPM nanoplates for different weight fractions of GPLs and distributions: **(a)** UD and **(b)** PD $(\mathrm{h} = 20\ \mathrm{nm}, \mathrm{a} = \mathrm{b} = 50\mathrm{h},\ \sigma_0 = 1\ \mathrm{N/m})$. The results corresponding to LD nanoplates are similar to that of the UD case.

deflection with and without considering flexoelectricity is more prominent than in figure 23(b) $(\sigma_0 = 1)$. Furthermore, if we compare the deflection reduction by considering only surface effect $(\mathrm{f}_{14} = 0)$, then also there is a reduction in maximum deflection of nanoplate due to pure surface effect, which is in coherence with the theory proposed by (Lu et al., 2006). For example, in a square UD-FGPM nanoplate $(\mathrm{h} = 20\ \mathrm{nm};\ \mathrm{a} = \mathrm{b} = 50\mathrm{h})$, pure surface effect reduces the deflection by 91.47 %, whereas the combined surface and flexoelectricity reduce it near about the same magnitude ~91.52 %.

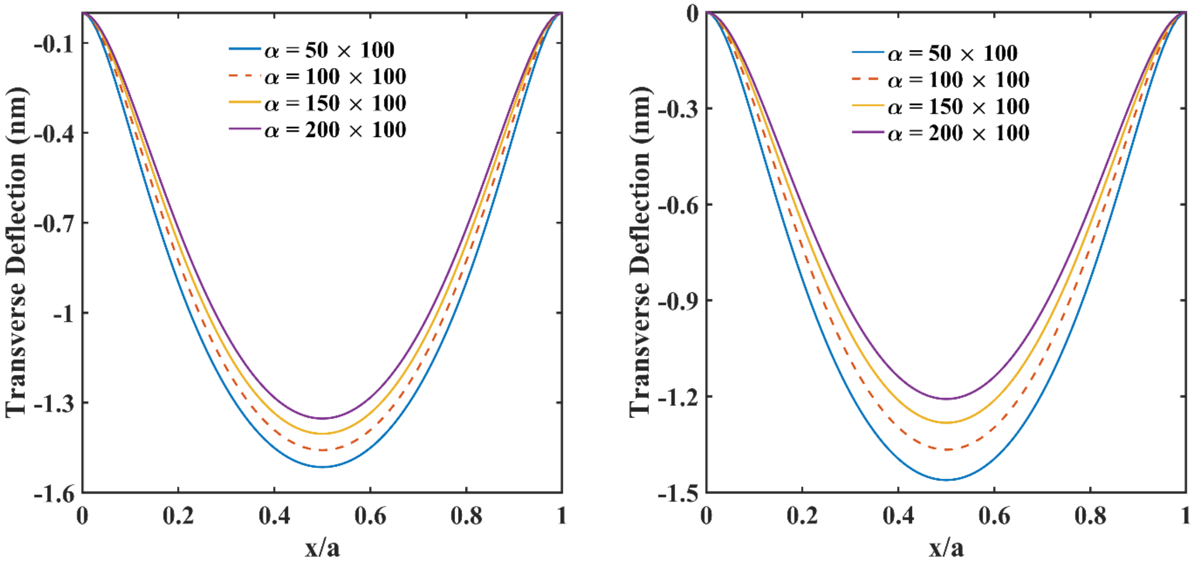

(a) (b)

Fig. 27. Variation of transverse deflection of flexo-surface FGPM nanoplates for various piezoelectric multiples and distributions: **(a)** UD and **(b)** PD. ($\mathrm{h = 20\,nm, a = b = 50h,\ \sigma_0 = 1\,N/m}$). The results corresponding to LD nanoplates are similar to that of the UD case.

Figure 24 shows the influences of the mechanical boundary conditions on the transverse deflection of flexo-surface FGPM nanoplate considering UD and PD distribution. In both cases ($\sigma_0 = 0$ and $\sigma_0 = 1$), it is apparent that CCCC nanoplate is stiffer than SSSS nanoplate as discussed in section 3.2.1. Another notable observation from this figure is that when we change residual surface stress from 0 to 1 $\mathrm{N/m}$, the percentage reduction of deflection in the SSSS surface nanoplate is much more than the CCCC plate which is true in the case of both distributions. Figure 25 represents a 3D representation of the deformed shape of the PD-FGPM plate for a better understanding of the deflection.

Figures 26 and 27 show the influences of the total weight fraction of GPLs in PVDF and piezoelectric multiple (α) in static deflection incorporating surface and flexoelectric effects. For the case of $\sigma_0 = 0$, these variations and trends are similar as presented in figures 18 and 19. For the sake of brevity, we have omitted those results here. It can be also observed that there is a reduction in transverse deflection of flexo-surface FGPM nanoplate with the increment in weight fraction of GPLs in PVDF matrix as well as increment in the value of piezoelectric multiples.

3.3 Dynamic response of FGPM nanoplates

In this section, we have performed free vibration analysis of FGPM structures with three different distributions of graphene nanoplatelets incorporating both flexoelectric and surface effects to carry out dynamic analysis. The material and dimensional parameters are same as that of the static case which is summarized in Table 5 and the Ritz method is implemented to extract all the dynamic results. As this is a free vibration case, the transverse load (q_0) is zero, i.e., dynamic analysis is independent of the externally applied load. Further analysis is performed in terms of mode (1, 1) natural eigenfrequency of the structure as this is fundamentally important for a range of applications.

Table 5. Resonant frequency (ω_{11}) (MHz) of SSSS flexoelectric FGPM nanoplates ($\mathrm{a/h} = 50$, $\mathrm{f}_{14} = 1 \times 10^{-7}\mathrm{C/m}$).

Distributions of FGM	**Thickness (h) (nm)**	**Navier solution**	**Ritz solution**
UD	20	29.7605	29.7662
	40	14.5722	14.5751
	60	9.6763	9.6782
	80	7.2471	7.2485
	100	5.7939	5.7949
LD	20	29.7939	29.7996
	40	14.5905	14.5933
	60	9.6887	9.6905
	80	7.2563	7.2578
	100	5.8014	5.8025
PD	20	33.6339	33.6406
	40	16.6312	16.6346
	60	11.0645	11.0665
	80	8.2923	8.2939
	100	6.6315	6.6328

In Table 5, the resonant frequencies of one SSSS flexoelectric FGPM nanoplate are compared for different thicknesses and GPLs distributions obtained from two different solutions – exact (Navier) and present (Ritz) solution. It demonstrates that the current Ritz solution is capable of producing findings with high level of accuracy (average % of error is 0.0193%). Having our semi-analytical framework validated with respect to exact solutions, we further investigate different critical aspects of free vibration and the effects of multiple influencing parameters. It can be noted in this context that the combined effect of surface and flexoelectricity becomes more noticeable with decreasing the dimensions of structures (thickness). It is observed that there is a significant increment in the magnitudes of eigenfrequencies due to the incorporation of surface effect and

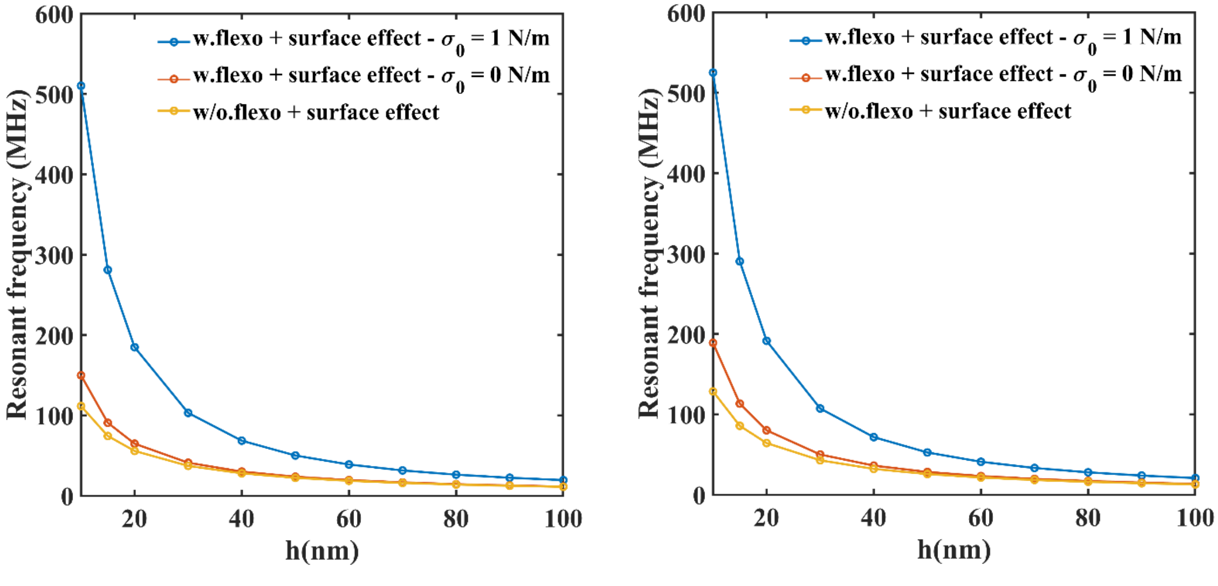

(a) (b)

Fig. 28. Variations of resonant frequency of FGPM nanoplates with thickness (h) considering different distributions of GPLs: **(a)** UD and **(b)** PD. (a = b = 50h). The results corresponding to LD nanoplates are similar to that of the UD case.

this percentage increment reduces in the higher mode of vibration. Our further analysis also reveals that, in case of PD-FGPM flexoelectric nanoplates ($h = 20$ nm, $a/h = 50$), an increase of 193.9% can be observed in the mode (1,1) whereas this percentage reduces to 76.4% in the mode (3,3) when the surface effect is considered. Figure 28 depicts the fluctuation in resonant frequency as a function of plate thickness for all three distributions that include surface, as well as with and without the flexoelectric effect. As discussed in earlier sections (refer to figure 22), the stiffness of PD-FGPM nanoplate is more as compared to UD and LD, and

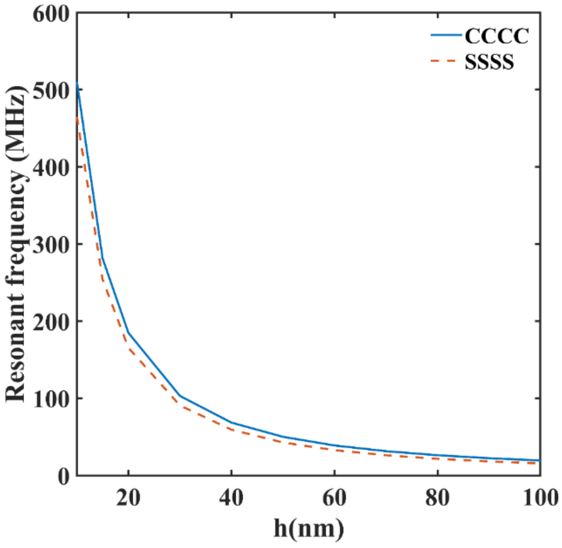

Fig. 29. Variation of resonant frequency of flexo-surface FGPM nanoplates with thickness (h) for CCCC and SSSS boundary conditions (UD, $a = b = 50h$, $\sigma_0 = 1$ N/m).

hence, it results in the highest natural frequency for PD distribution considering all residual surface stresses. For example, in case of $\sigma_0 = 1\ \mathrm{N/m}$, a square UD or LD-FGPM nanoplate ($\mathrm{h} = 15\ \mathrm{nm};\ \mathrm{a/h} = 50$) shows 281.1 MHz fundamental frequency for mode (1,1), whereas in case of PD-FGPM, it is 290.3 MHz. From figure 28, it is observed, due to the incorporation of surface and flexoelectricity, the natural frequency of FGPM nanoplate increases, and the results are in very good agreement with existing literature (Ebrahimi and Barati, 2019). Nanoplate with non-zero residual surface stress ($\sigma_0 = 1\ \mathrm{N/m}$) gives a higher resonant frequency than that of zero residual surface stress. For example, in the case of $\sigma_0 = 1\ \mathrm{N/m}$ in a square PD-FGPM nanoplate ($\mathrm{h} = 15\ \mathrm{nm};\ \mathrm{a/h} = 50$), the fundamental frequency for mode (1,1) is 290.3 MHz, whereas it is 113.4 MHz for $\sigma_0 = 0$. Similar trend of results were observed in the existing literature on annular nanoplate (Ghorbanpour Arani et al., 2021). In figure 28, the difference among these three curves reduces with the increase of thickness. This is due to the size-dependent effect of nano-scaled structures.

Figure 29 demonstrates the effect of mechanical boundary conditions such as SSSS and CCCC nanoplate on its resonant frequency. Here, the plate aspect ratio and residual surface stress are 50 and 1 N/m, respectively. Like conventional plates, the eigenfrequency in the case of CCCC plate is always higher than that of SSSS plate. Figure 30 represents the first four mode shapes of a square PD-FGPM nanoplate ($\mathrm{h} = 20\ \mathrm{nm};\ \mathrm{a/h} = 50$) with CCCC and SSSS boundary conditions incorporating both surface and flexoelectric effects. Figure 31 shows the variation of resonant frequency in terms of plate thickness for various aspect ratios and weight fractions of GPLs in the PVDF matrix. For instance, increasing aspect ratio ($\mathrm{a/h}$) leads to a decrease in the frequencies of the UD-FGPM nanoplate. The same trend of results is also observed in the case of other remaining distributions. Incorporating more graphene platelets within the PVDF matrix as reinforcement leads to an increase in its overall stiffness. Therefore, we get higher values of natural frequency in the case of $\mathrm{W}_{\mathrm{GPL}}^{\mathrm{t}} = 4\%$ than that of $\mathrm{W}_{\mathrm{GPL}}^{\mathrm{t}} = 1\%$. For example, in the case of $\sigma_0 = 1\ \mathrm{N/m}$, a square UD-FGPM nanoplate ($\mathrm{h} = 40\ \mathrm{nm};\ \mathrm{a/h} = 50$) shows an increase of ~20.01 % in natural frequency if we increase GPL’s percentage from 1% to 4%. This percentage increases with the aspect ratio, indication a coupled effect between GPL’s percentage and aspect ratio.

Physical realization of the nano-scale structures, as discussed in this paper, is of crucial importance. From an experimental viewpoint, it is important to find out an appropriate fabrication technique to manufacture the nanocomposite structures. Nanofabrication techniques such as layer-by-layer (LbL) assembly, dispersion and solution blending route methods are widely used to fabricate multifunctional thin films (Gamboa et al., 2010). For instance, the assemblies of multi-layers of graphene oxide (GO) and polyethylenimine (PEI) were presented by tailoring the thickness of assemblies by varying the number of GO layers. In the case of bi-layer of GO and PEI, the thickness of assembly near about ~4.5-5 nm was achieved. In some other studies (Yang et al., 2013; Prolongo et al., 2014; Tzeng et al., 2015; Prolongo et al., 2018), the thickness of assembly was achieved in the range of 8-10 nm using 4 to 30 GPLs. Using all these techniques,

CCCC nanoplate	SSSS nanoplate
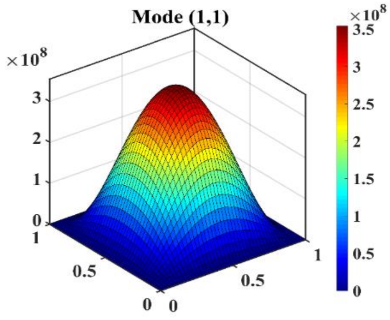 **(a)**	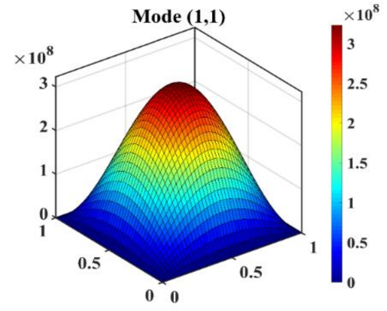 **(e)**
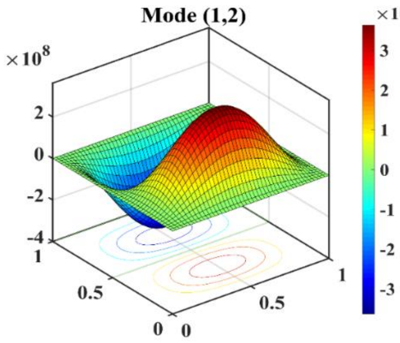 **(b)**	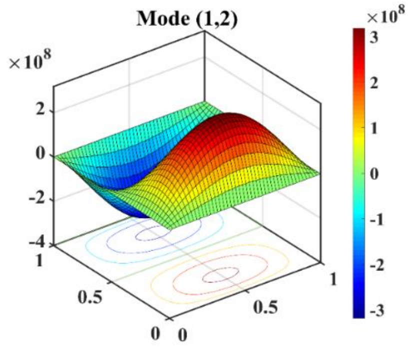 **(f)**
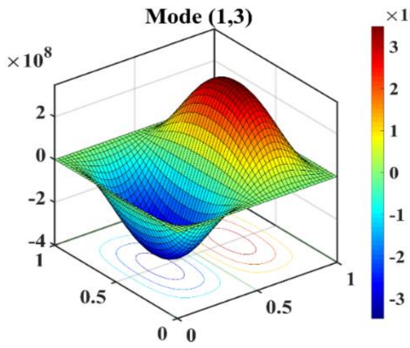 **(c)**	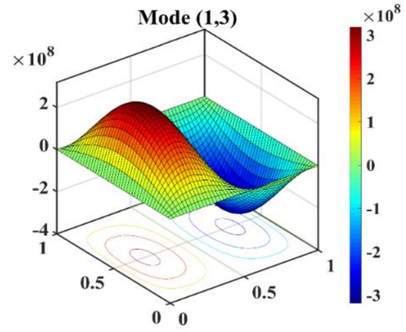 **(g)**
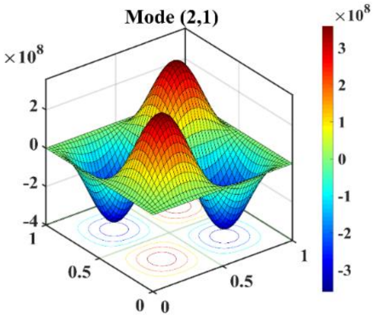 **(d)**	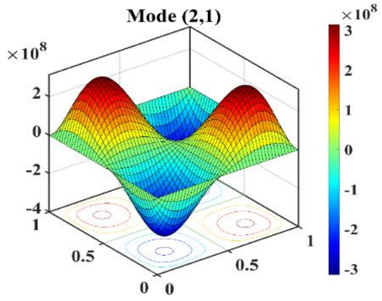 **(h)**

Fig. 30. Mode shapes of flexo-surface FGPM nanoplates with CCCC and SSSS boundary conditions $(\mathrm{PD}, \mathrm{h} = 20\mathrm{nm},\ \mathrm{a} = \mathrm{b} = 50\mathrm{h}\,, \sigma_0 = 1\ \mathrm{N/m})$.

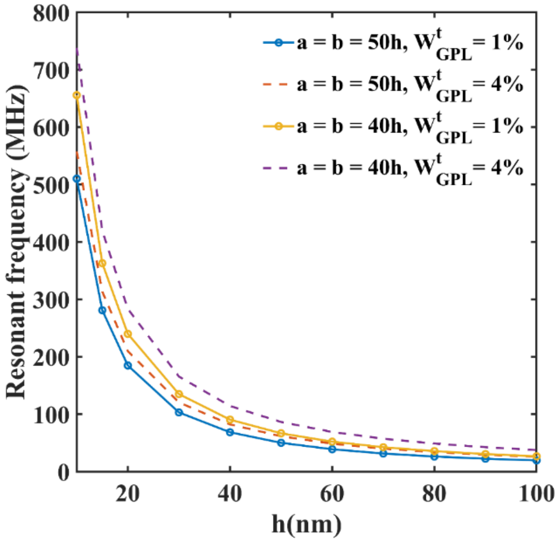

Fig. 31. Variation of resonant frequency of flexo-surface FGPM nanoplates with thickness (h) for different aspect ratios and GPL weight fractions (UD, $\sigma_0 = 1\ \mathrm{N/m}$). Here a clamped boundary condition is considered.

the fabrication of thin nanocomposite can be achieved on the order of nanometer. Therefore, one can use these techniques to fabricate graphene-based nanocomposite and achieve significant electromechanical response considering flexoelectric and surface effects.

In view of the analytical and numerical study, in the present study, the GPLs are assumed as rectangular-shaped solid reinforcement of average width w_{GPL}, length l_{GPL} and thickness t_{GPL}, and the values of these parameters are taken 1.8 nm, 3 nm, and 0.7 nm, respectively. We used material properties and geometrical parameters of GPLs and PVDF from existing literature which are given in Table 4. Moreover, we make use of 'classical Kirchhoff plate theory' (Eq. 15) which generally gives accurate results if the concerned plate is thin ($a/h \geq 20$). Now for instance, if we take a square plate with aspect ratio ($a/h = 100$) and length (1000 nm), then it is evident that the GPLs with thickness 0.7 nm can easily be accommodated within the plate of 10 nm thickness.

4. Concluding remarks

The coupled electromechanical behaviour of graphene reinforced functionally graded piezoelectric material (FGPM) nanoplates is explored by taking into account the surface and flexoelectricity effects concerning the static and dynamic responses. Owing to inhomogeneous strain and high surface-to-volume ratio in nanostructures, it is important to account for the flexoelectricity as well as surface effect while analyzing the size-dependent electromechanical responses of nano-scale piezoelectric materials. An efficient semi-analytical framework is developed here for the FGPM nanoplates under the open-circuit condition, wherein the single term extended Kantorovich method (EKM) is implemented for static analysis and the Ritz method is adopted for dynamic analysis. The numerical results are extensively validated with existing literature for checking the accuracy of the present model. It is noted that the novel EKM based framework for graphene reinforced FGPM nanoplates provides rapid convergence for investigating the role of surface and flexoelectricity effects, while the Ritz method is capable of predicting accurate dynamic behavior of the system incorporating both the effects.

Based on the unified semi-analytical framework, a comprehensive investigation is carried out on static deflection and free vibration considering different distributions of graphene platelets in FGPM nanoplates such as linear distribution (LD), uniform distribution (UD), and parabolic distribution (PD). In all cases, the parabolic distribution exhibits the stiffest behavior and higher natural frequency compared to the other distributions. In this study, the electromechanical response of nanoplates is investigated considering different crucial parameters such as plate thicknesses, aspect ratios, flexoelectric coefficients, piezoelectric multiples and weight fraction of graphene platelets along with different boundary conditions. Our findings reveal that the static deflection and dynamic resonance of FGPM are enhanced significantly due to consideration of flexoelectricity and surface effects, leading to the realization that such effects cannot be neglected. Further, these electromechanical effects can be exploited in designing novel materials and devices for active response control and energy harvesting. The electromechanical effects are found to be more pronounced for nanoplates of lesser thickness, and these diminish as plate thickness increases, indicating a novel size-dependent behaviour that could potentially be of significant importance for micro and nano architected materials. The current investigation further reveals that the stiffening behavior is greatly dependent on the sign and magnitude of residual surface stress. In the absence of surface effect, FG-PD shows a high correlation to the thickness change as compared to FG-UD and FG-LD. However, in the presence of a surface effect, this correlation can be modulated in different distributions as per application-specific demands. In the presence of non-zero residual stresses, the static and dynamic responses for different FGPM distributions are dependent on the in-plane dimensions of the plates in addition to thickness. Such numerical outcomes essentially open up the avenues of prospective exploitation and augmentation of the electromechanical responses in an expanded design space including the factors like open- and close-circuit condition, strain/electric field gradient, electrical and mechanical loading as well as converse piezoelectricity and flexoelectricity. With the recent advances in nano-scale manufacturing and experimental capabilities, this article will provide the necessary physical insights in modeling the size-dependent electromechanical coupling in multifunctional materials, systems and devices for applications in sensors, actuators, nanogenerators, active controllers, nano-robotics and energy harvesters.

Acknowledgments

SN acknowledges the financial support through initiation grant from University of Southampton. KBS would like to thank IIT Bombay for the Institute Post-doctoral Fellowship (IPDF). TM would like to acknowledge the financial support from Science and Engineering Research Board (Grant no. SRG/2020/001398).

Conflict of Interest

The authors declare no conflict of interest.

Data availability statement

All relevant data have been included either in the manuscript or it will be made available upon reasonable requests.

ORCID ID

Susmita Naskar https://orcid.org/0000-0003-3294-8333
Kishor Shingare https://orcid.org/0000-0002-8255-9849
Soumyadeep Mondal https://orcid.org/0000-0002-3368-7828
Tanmoy Mukhopadhyay https://orcid.org/0000-0002-0778-6515

Appendix A

The stiffness coefficients and their algebraic expressions in Eq. (22) are expressed as follows:

$$A_{11} = \int_{-h/2}^{h/2} \left(z^2 c_{11}(z) + z e_{31}(z) f_{1z}(z)\right) dz \qquad B_{11} = \int_{-h/2}^{h/2} \left(z c_{11}(z) + e_{31}(z) f_{1z}(z)\right) dz$$

$$A_{12} = \int_{-h/2}^{h/2} \left(z^2 c_{12}(z) + z e_{31}(z) f_{2z}(z)\right) dz \qquad B_{12} = \int_{-h/2}^{h/2} \left(z c_{12}(z) + e_{31}(z) f_{2z}(z)\right) dz$$

$$A_{21} = \int_{-h/2}^{h/2} \left(z^2 c_{12}(z) + z e_{32}(z) f_{1z}(z)\right) dz \qquad B_{21} = \int_{-h/2}^{h/2} \left(z c_{12}(z) + e_{32}(z) f_{1z}(z)\right) dz$$

$$A_{22} = \int_{-h/2}^{h/2} \left(z^2 c_{22}(z) + z e_{32}(z) f_{2z}(z)\right) dz \qquad B_{22} = \int_{-h/2}^{h/2} \left(z c_{22}(z) + e_{32}(z) f_{2z}(z)\right) dz$$

$$A_{66} = \int_{-h/2}^{h/2} \left(z^2 c_{66}(z)\right) dz \qquad B_{66} = \int_{-h/2}^{h/2} \left(z c_{66}(z)\right) dz$$

$$A_{11}^{f} = \int_{-h/2}^{h/2} f_{14}(z)\, f_{1z}(z) dz \qquad B^{+} = 2\left(\frac{h}{2}\right) c_{66}^{s}\left(\frac{h}{2}\right)$$

$$A_{21}^{f} = \int_{-h/2}^{h/2} f_{14}(z)\, f_{1z}(z) dz \qquad B^{-} = 2\left(-\frac{h}{2}\right) c_{66}^{s}\left(-\frac{h}{2}\right)$$

$$A_{01}^{+} = \frac{h}{2}\sigma^{0}$$

$$B_{01}^{+} = \sigma^{0}$$

$$A_{01}^{-} = -\frac{h}{2}\sigma^{0}$$

$$B_{01}^{-} = \sigma^{0}$$

$$A_{11}^{+} = \left(\frac{h}{2}\right)^{2} c_{11}^{s}\left(\frac{h}{2}\right) + \left(\frac{h}{2}\right) f_{1z}\left(\frac{h}{2}\right) e_{31}^{s}\left(\frac{h}{2}\right)$$

$$B_{11}^{+} = \left(\frac{h}{2}\right) c_{11}^{s}\left(\frac{h}{2}\right) + f_{1z}\left(\frac{h}{2}\right) e_{31}^{s}\left(\frac{h}{2}\right)$$

$$A_{21}^{+} = \left(\frac{h}{2}\right)^{2} c_{12}^{s}\left(\frac{h}{2}\right) + \left(\frac{h}{2}\right) f_{2z}\left(\frac{h}{2}\right) e_{31}^{s}\left(\frac{h}{2}\right)$$

$$B_{21}^{+} = \left(\frac{h}{2}\right) c_{12}^{s}\left(\frac{h}{2}\right) + f_{2z}\left(\frac{h}{2}\right) e_{31}^{s}\left(\frac{h}{2}\right)$$

$$\begin{aligned} A_{11}^{-} = {} & \left(-\frac{h}{2}\right)^{2} c_{11}^{s}\left(-\frac{h}{2}\right) \\ & + \left(-\frac{h}{2}\right) f_{1z}\left(-\frac{h}{2}\right) e_{31}^{s}\left(-\frac{h}{2}\right) \end{aligned}$$

$$B_{11}^{-} = \left(-\frac{h}{2}\right) c_{11}^{s}\left(-\frac{h}{2}\right) + f_{1z}\left(-\frac{h}{2}\right) e_{31}^{s}\left(-\frac{h}{2}\right)$$

$$\begin{aligned} A_{21}^{-} = {} & \left(-\frac{h}{2}\right)^{2} c_{12}^{s}\left(-\frac{h}{2}\right) \\ & + \left(-\frac{h}{2}\right) f_{2z}\left(-\frac{h}{2}\right) e_{31}^{s}\left(-\frac{h}{2}\right) \end{aligned}$$

$$B_{21}^{-} = \left(-\frac{h}{2}\right) c_{12}^{s}\left(-\frac{h}{2}\right) + f_{2z}\left(-\frac{h}{2}\right) e_{31}^{s}\left(-\frac{h}{2}\right)$$

$$A_{02}^{+} = \frac{h}{2}\sigma^{0}$$

$$B_{02}^{+} = \sigma^{0}$$

$$A_{02}^{+} = -\frac{h}{2}\sigma^{0}$$

$$B_{02}^{-} = \sigma^{0}$$

$$A_{12}^{+} = \left(\frac{h}{2}\right)^{2} c_{21}^{s}\left(\frac{h}{2}\right) + \left(\frac{h}{2}\right) f_{1z}\left(\frac{h}{2}\right) e_{32}^{s}\left(\frac{h}{2}\right)$$

$$B_{12}^{+} = \left(\frac{h}{2}\right) c_{21}^{s}\left(\frac{h}{2}\right) + f_{1z}\left(\frac{h}{2}\right) e_{32}^{s}\left(\frac{h}{2}\right)$$

$$A_{22}^{+} = \left(\frac{h}{2}\right)^{2} c_{22}^{s}\left(\frac{h}{2}\right) + \left(\frac{h}{2}\right) f_{2z}\left(\frac{h}{2}\right) e_{32}^{s}\left(\frac{h}{2}\right)$$

$$B_{22}^{+} = \left(\frac{h}{2}\right) c_{22}^{s}\left(\frac{h}{2}\right) + f_{2z}\left(\frac{h}{2}\right) e_{32}^{s}\left(\frac{h}{2}\right)$$

$$\begin{aligned} A_{12}^{-} = {} & \left(-\frac{h}{2}\right)^{2} c_{21}^{s}\left(-\frac{h}{2}\right) \\ & + \left(-\frac{h}{2}\right) f_{1z}\left(-\frac{h}{2}\right) e_{32}^{s}\left(-\frac{h}{2}\right) \end{aligned}$$

$$B_{12}^{-} = \left(-\frac{h}{2}\right) c_{21}^{s}\left(-\frac{h}{2}\right) + f_{1z}\left(-\frac{h}{2}\right) e_{32}^{s}\left(-\frac{h}{2}\right)$$

$$\begin{aligned} A_{22}^{+} = {} & \left(-\frac{h}{2}\right)^{2} c_{22}^{s}\left(-\frac{h}{2}\right) \\ & + \left(-\frac{h}{2}\right) f_{2z}\left(-\frac{h}{2}\right) e_{32}^{s}\left(-\frac{h}{2}\right) \end{aligned}$$

$$B_{22}^{-} = \left(-\frac{h}{2}\right) c_{22}^{s}\left(-\frac{h}{2}\right) + f_{2z}\left(-\frac{h}{2}\right) e_{32}^{s}\left(-\frac{h}{2}\right)$$

$$A_0^+ = \frac{h}{2}\sigma^0 \qquad B_0^+ = \sigma^0$$

$$A_0^- = -\frac{h}{2}\sigma^0 \qquad B_0^- = \sigma^0$$

$$A^+ = 2\left(\frac{h}{2}\right)^2 c_{66}^s\left(\frac{h}{2}\right) \qquad A^- = 2\left(-\frac{h}{2}\right)^2 c_{66}^s\left(-\frac{h}{2}\right)$$

Appendix B

All the coefficients (H_i) of each term and their algebraic expressions in Eq. (24) are expressed as follows:

$$H_1 = A_{11} + A_{11}^f + A_{11}^+ + A_{11}^-$$

$$H_2 = A_{22} + A_{21}^f + A_{22}^+ + A_{22}^-$$

$$H_3 = A_{21} + A_{12} + A_{21}^f + A_{11}^f + 4A_{66} + A_{21}^+ + A_{21}^- + A_{12}^+ + A_{12}^- + 2A^+ + 2A^-$$

Here, H_4 , H_5 , H_6 and H_7 are non-linear terms which are expressed as follows:

$$H_4 = B_{11} + B_{11}^+ + B_{11}^-$$

$$H_5 = B_{22} + B_{22}^+ + B_{22}^-$$

$$H_6 = B_{12} + B_{21}^+ + B_{21}^- + B_{21} + B_{12} + B_{12}^+ + B_{12}^-$$

$$H_7 = 4B_{66} + 2B^+ + 2B^-$$

$$H_8 = B_{01}^+ + B_{01}^-$$

$$H_9 = B_{02}^+ + B_{02}^-$$

$$H_{10} = 2B_0^+ + 2B_0^-$$

The coefficients and their algebraic expressions in Eq. (32) are expressed as:

$$D_1 = A_{11} + A_{11}^f + A_{11}^+ + A_{11}^-$$

$$D_2 = A_{22} + A_{21}^f + A_{22}^+ + A_{22}^-$$

$$D_3 = A_{12} + A_{21}^+ + A_{21}^- + A_{21}^f$$

$$D_4 = A_{21} + A_{12}^+ + A_{12}^- + A_{11}^f$$

$$D_5 = 4A_{66} + 2A^{+} + 2A^{+}$$

$$D_{15} = B_{01}^{+} + B_{01}^{-}$$

$$D_{16} = B_{02}^{+} + B_{02}^{-}$$

$$D_{17} = B_{0}^{+} + B_{0}^{-} = D_{18}$$

References

Abolhasani, M.M., Shirvanimoghaddam, K., Naebe, M., 2017. PVDF/graphene composite nanofibers with enhanced piezoelectric performance for development of robust nanogenerators. Compos. Sci. Technol. 138, 49–56. https://doi.org/10.1016/j.compscitech.2016.11.017

Aitken, Z.H., Fan, H., El-Awady, J.A., Greer, J.R., 2015. The effect of size, orientation and alloying on the deformation of AZ31 nanopillars. J. Mech. Phys. Solids 76, 208–223. https://doi.org/10.1016/j.jmps.2014.11.014

Akbarzadeh Khorshidi, M., 2020. Validation of weakening effect in modified couple stress theory: Dispersion analysis of carbon nanotubes. Int. J. Mech. Sci. 170. https://doi.org/10.1016/j.ijmecsci.2019.105358

Akbarzadeh Khorshidi, M., 2018. The material length scale parameter used in couple stress theories is not a material constant. Int. J. Eng. Sci. 133, 15–25. https://doi.org/10.1016/j.ijengsci.2018.08.005

Arefi, M., Mohammad-Rezaei Bidgoli, E., Dimitri, R., Tornabene, F., 2018. Free vibrations of functionally graded polymer composite nanoplates reinforced with graphene nanoplatelets. Aerosp. Sci. Technol. 81, 108–117. https://doi.org/10.1016/j.ast.2018.07.036

Baskaran, S., He, X., Chen, Q., Fu, J.Y., 2011. Experimental studies on the direct flexoelectric effect in α - phase polyvinylidene fluoride films. Appl. Phys. Lett. 98. https://doi.org/10.1063/1.3599520

Beeby, S.P., Tudor, M.J., White, N.M., 2006. Energy harvesting vibration sources for microsystems applications. Meas. Sci. Technol. 17. https://doi.org/10.1088/0957-0233/17/12/R01

Beheshti-Aval, S.B., Lezgy-Nazargah, M., 2010. A finite element model for composite beams with piezoelectric layers using a sinus model. J. Mech. 26, 249–258. https://doi.org/10.1017/S1727719100003105

Chan, K.T., Pu, Z.Y., 2011. The dispersion characteristics of the waves propagating in a spinning single-walled carbon nanotube. Sci. China Physics, Mech. Astron. 54, 1854–1865. https://doi.org/10.1007/s11433-011-4476-9

Chandratre, S., Sharma, P., 2012. Coaxing graphene to be piezoelectric. Appl. Phys. Lett. 100. https://doi.org/10.1063/1.3676084

Chen, D., Yang, J., Kitipornchai, S., 2017. Nonlinear vibration and postbuckling of functionally graded graphene reinforced porous nanocomposite beams. Compos. Sci. Technol. 142, 235–245. https://doi.org/10.1016/j.compscitech.2017.02.008

Curie, J., Curie, P., 1880. Développement par compression de l’électricité polaire dans les cristaux hémièdres à faces inclinées. Bull. la Société minéralogique Fr. 3, 90–93. https://doi.org/10.3406/bulmi.1880.1564

Dang, Z.M., Lin, Y.H., Nan, C.W., 2003. Novel Ferroelectric Polymer Composites with High Dielectric Constants. Adv. Mater. 15, 1625–1629. https://doi.org/10.1002/adma.200304911

Deng, Q., Kammoun, M., Erturk, A., Sharma, P., 2014. Nanoscale flexoelectric energy harvesting. Int. J. Solids Struct. 51, 3218–3225. https://doi.org/10.1016/j.ijsolstr.2014.05.018

Ebrahimi, F., Barati, M.R., 2019. Dynamic modeling of embedded nanoplate systems incorporating flexoelectricity and surface effects. Microsyst. Technol. 25, 175–187. https://doi.org/10.1007/s00542-018-3946-7

Ebrahimi, F., Barati, M.R., 2017. Static stability analysis of embedded flexoelectric nanoplates considering surface effects. Appl. Phys. A Mater. Sci. Process. 123. https://doi.org/10.1007/s00339-017-1265-y

Ebrahimi, F., Hosseini, S.H.S., 2020. Investigation of flexoelectric effect on nonlinear forced vibration of piezoelectric/functionally graded porous nanocomposite resting on viscoelastic foundation. J. Strain Anal. Eng. Des. 55, 53–68. https://doi.org/10.1177/0309324719890868

Feng, C., Kitipornchai, S., Yang, J., 2017. Nonlinear bending of polymer nanocomposite beams reinforced with non-uniformly distributed graphene platelets (GPLs). Compos. Part B Eng. 110, 132–140. https://doi.org/10.1016/j.compositesb.2016.11.024

Ghobadi, A., Beni, Y.T., Golestanian, H., 2020. Nonlinear thermo-electromechanical vibration analysis of size-dependent functionally graded flexoelectric nano-plate exposed magnetic field. Arch. Appl. Mech. 90, 2025–2070. https://doi.org/10.1007/s00419-020-01708-0

Ghobadi, A., Golestanian, H., Beni, Y.T., Żur, K.K., 2021a. On the size-dependent nonlinear thermo-electro-mechanical free vibration analysis of functionally graded flexoelectric nano-plate. Commun. Nonlinear Sci. Numer. Simul. 95. https://doi.org/10.1016/j.cnsns.2020.105585

Ghobadi, A., Tadi Beni, Y., Kamil Żur, K., 2021b. Porosity distribution effect on stress, electric field and nonlinear vibration of functionally graded nanostructures with direct and inverse flexoelectric phenomenon. Compos. Struct. 259. https://doi.org/10.1016/j.compstruct.2020.113220

Ghorbanpour Arani, A., Soltan Arani, A.H., Haghparast, E., 2021. Flexoelectric and surface effects on vibration frequencies of annular nanoplate. Indian J. Phys. 95, 2063–2083. https://doi.org/10.1007/s12648-020-01854-9

Gurtin, M.E., Ian Murdoch, A., 1975. A continuum theory of elastic material surfaces. Arch. Ration. Mech. Anal. 57, 291–323. https://doi.org/10.1007/BF00261375

Hamdia, K.M., Ghasemi, H., Zhuang, X., Alajlan, N., Rabczuk, T., 2018. Sensitivity and uncertainty analysis for flexoelectric nanostructures. Comput. Methods Appl. Mech. Eng. 337, 95–109. https://doi.org/10.1016/j.cma.2018.03.016

He, J., Lilley, C.M., 2008. Surface effect on the elastic behavior of static bending nanowires. Nano Lett. 8, 1798–1802. https://doi.org/10.1021/nl0733233

Hosseini, M., Jamalpoor, A., Fath, A., 2017. Surface effect on the biaxial buckling and free vibration of FGM nanoplate embedded in visco-Pasternak standard linear solid-type of foundation. Meccanica 52, 1381–1396. https://doi.org/10.1007/s11012-016-0469-0

Hu, X., Zhou, Y., Liu, J., Chu, B., 2018. Improved flexoelectricity in PVDF/barium strontium titanate (BST) nanocomposites. J. Appl. Phys. 123. https://doi.org/10.1063/1.5022650

Huang, G.Y., Yu, S.W., 2006. Effect of surface piezoelectricity on the electromechanical behaviour of a piezoelectric ring. Phys. Status Solidi Basic Res. 243. https://doi.org/10.1002/pssb.200541521

Jang, D., Meza, L.R., Greer, F., Greer, J.R., 2013. Fabrication and deformation of three-dimensional hollow ceramic nanostructures. Nat. Mater. https://doi.org/10.1038/nmat3738

Jones, R., Milne, B.J., 1976. Application of the extended Kantorovich method to the vibration of clamped rectangular plates. J. Sound Vib. 45, 309–316. https://doi.org/10.1016/0022-460X(76)90390-4

Kapuria, S., Kumari, P., 2011. Extended Kantorovich method for three-dimensional elasticity solution of laminated composite structures in cylindrical bending. J. Appl. Mech. Trans. ASME 78, 1–8. https://doi.org/10.1115/1.4003779

Kapuria, S., Kumari, P., 2012. Multiterm extended kantorovich method for three-dimensional elasticity solution of laminated plates. J. Appl. Mech. Trans. ASME 79, 1–9. https://doi.org/10.1115/1.4006495

Kapuria, S., Kumari, P., 2013. Extended Kantorovich method for coupled piezoelasticity solution of piezolaminated plates showing edge effects. Proc. R. Soc. A Math. Phys. Eng. Sci. 469, 20120565. https://doi.org/10.1098/rspa.2012.0565

Karsh, P.K., Mukhopadhyay, T., Chakraborty, S., Naskar, S., Dey, S., 2019. A hybrid stochastic sensitivity analysis for low-frequency vibration and low-velocity impact of functionally graded plates. Compos. Part B Eng. 176, 107221. https://doi.org/10.1016/j.compositesb.2019.107221

Kerr, A.D., Alexander, H., 1968. An application of the extended Kantorovich method to the stress analysis of a clamped rectangular plate. Acta Mech. 6, 180–196. https://doi.org/10.1007/BF01170382

Kiani, Y., 2018. Isogeometric large amplitude free vibration of graphene reinforced laminated plates in thermal environment using NURBS formulation. Comput. Methods Appl. Mech. Eng. 332, 86–101. https://doi.org/10.1016/j.cma.2017.12.015

Komijani, M., Reddy, J.N., Eslami, M.R., 2014. Nonlinear analysis of microstructure-dependent functionally graded piezoelectric material actuators. J. Mech. Phys. Solids 63, 214–227. https://doi.org/10.1016/j.jmps.2013.09.008

Kumar, A., Kiran, R., Kumar, R., Chandra Jain, S., Vaish, R., 2018. Flexoelectric effect in functionally graded materials: A numerical study. Eur. Phys. J. Plus 133. https://doi.org/10.1140/epjp/i2018-11976-1

Kumari, P., Shakya, A.K., 2017. Two-dimensional Solution of Piezoelectric Plate Subjected to Arbitrary Boundary Conditions using Extended Kantorovich Method, in: Procedia Engineering. pp. 1523–1530. https://doi.org/10.1016/j.proeng.2016.12.236

Kundalwal, S.I., Shingare, K.B., 2020. Electromechanical response of thin shell laminated with flexoelectric composite layer. Thin-Walled Struct. 157. https://doi.org/10.1016/j.tws.2020.107138

Kundalwal, S. I., Shingare, K.B., Gupta, M., 2020. Flexoelectric effect on electric potential in piezoelectric graphene-based composite nanowire: Analytical and numerical modelling. Eur. J. Mech. A/Solids 84. https://doi.org/10.1016/j.euromechsol.2020.104050

Lezgy-Nazargah, M., Vidal, P., Polit, O., 2013. An efficient finite element model for static and dynamic analyses of functionally graded piezoelectric beams. Compos. Struct. 104, 71–84. https://doi.org/10.1016/j.compstruct.2013.04.010

Li, A., Wang, B., Yang, S., 2021. On some basic aspects of flexoelectricity in the mechanics of materials. Int. J. Eng. Sci. 166. https://doi.org/10.1016/j.ijengsci.2021.103499

Li, Z., He, Y., Lei, J., Guo, S., Liu, D., Wang, L., 2018. A standard experimental method for determining the material length scale based on modified couple stress theory. Int. J. Mech. Sci. 141, 198–205. https://doi.org/10.1016/j.ijmecsci.2018.03.035

Liang, X., Hu, S., Shen, S., 2013. Bernoulli-Euler dielectric beam model based on strain-gradient effect. J. Appl. Mech. Trans. ASME 80. https://doi.org/10.1115/1.4023022

Lippmann, G., 1881. Principe de la conservation de l'électricité, ou second principe de la théorie des phénomènes électriques. J. Phys. Théorique Appliquée 10, 381–394. https://doi.org/10.1051/jphystap:0188100100038100

Liu, C., Rajapakse, R.K.N.D., 2013. A size-dependent continuum model for nanoscale circular plates. IEEE Trans. Nanotechnol. 12, 13–20. https://doi.org/10.1109/TNANO.2012.2224880

Liu, C., Rajapakse, R.K.N.D., 2010. Continuum models incorporating surface energy for static and dynamic response of nanoscale beams. IEEE Trans. Nanotechnol. 9, 422–431. https://doi.org/10.1109/TNANO.2009.2034142

Liu, C., Rajapakse, R.K.N.D., Phani, A.S., 2011. Finite element modeling of beams with surface energy effects. J. Appl. Mech. Trans. ASME 78. https://doi.org/10.1115/1.4003363

Lu, P., He, L.H., Lee, H.P., Lu, C., 2006. Thin plate theory including surface effects. Int. J. Solids Struct. 43, 4631–4647. https://doi.org/10.1016/j.ijsolstr.2005.07.036

Mao, J.J., Zhang, W., 2018. Linear and nonlinear free and forced vibrations of graphene reinforced piezoelectric composite plate under external voltage excitation. Compos. Struct. 203, 551–565. https://doi.org/10.1016/j.compstruct.2018.06.076

Mehralian, F., Tadi Beni, Y., Karimi Zeverdejani, M., 2017. Nonlocal strain gradient theory calibration using molecular dynamics simulation based on small scale vibration of nanotubes. Phys. B Condens. Matter 514, 61–69. https://doi.org/10.1016/j.physb.2017.03.030

Miller, R.E., Shenoy, V.B., 2000. Size-dependent elastic properties of nanosized structural elements. Nanotechnology 11, 139–147. https://doi.org/10.1088/0957-4484/11/3/301

Naskar, S., 2018a. Spatial Variability Characterisation of Laminated Composites. University of Aberdeen. https://doi.org/10.13140/RG.2.2.17696.84483

Naskar, S., Mukhopadhyay, T., Sriramula, S., 2018b. Probabilistic micromechanical spatial variability quantification in laminated composites. Compos. Part B Eng. 151, 291–325. https://doi.org/10.1016/j.compositesb.2018.06.002

Naskar, S., Mukhopadhyay, T., Sriramula, S., 2019. Spatially varying fuzzy multi-scale uncertainty propagation in unidirectional fibre reinforced composites. Compos. Struct. 209, 940–967. https://doi.org/10.1016/j.compstruct.2018.09.090

Naskar, S., Mukhopadhyay, T., Sriramula, S., Adhikari, S., 2017. Stochastic natural frequency analysis of damaged thin-walled laminated composite beams with uncertainty in micromechanical properties. Compos. Struct. 160, 312–334. https://doi.org/10.1016/j.compstruct.2016.10.035

Pan, X., Yu, S., Feng, X., 2011. A continuum theory of surface piezoelectricity for nanodielectrics. Sci. China Physics, Mech. Astron. 54, 564–573. https://doi.org/10.1007/s11433-011-4275-3

Reddy, J.N., 2006. Theory and Analysis of Elastic Plates and Shells, Theory and Analysis of Elastic Plates and Shells. https://doi.org/10.1201/9780849384165

Reddy, J.N., 2003. Mechanics of Laminated Composite Plates and Shells, Mechanics of Laminated Composite Plates and Shells. https://doi.org/10.1201/b12409

Reddy, J.N., 1999. On laminated composite plates with integrated sensors and actuators. Eng. Struct. 21, 568–593. https://doi.org/10.1016/S0141-0296(97)00212-5

Reddy, J.N., Cheng, Z.Q., 2001. Three-dimensional solutions of smart functionally graded plates. J. Appl. Mech. Trans. ASME 68, 234–241. https://doi.org/10.1115/1.1347994

Sapsathiarn, Y., Rajapakse, R.K.N.D., 2017. Static and dynamic analyses of nanoscale rectangular plates incorporating surface energy. Acta Mech. 228, 2849–2863. https://doi.org/10.1007/s00707-015-1521-1

Sharma, S., Kumar, R., Talha, M., Vaish, R., 2021. Flexoelectric Poling of Functionally Graded Ferroelectric Materials. Adv. Theory Simulations 4. https://doi.org/10.1002/adts.202000158

Shen, H.S., Lin, F., Xiang, Y., 2017a. Nonlinear bending and thermal postbuckling of functionally graded graphene-reinforced composite laminated beams resting on elastic foundations. Eng. Struct. 140, 89–97. https://doi.org/10.1016/j.engstruct.2017.02.069

Shen, H.S., Xiang, Y., Lin, F., Hui, D., 2017b. Buckling and postbuckling of functionally graded graphene-reinforced composite laminated plates in thermal environments. Compos. Part B Eng. 119, 67–78. https://doi.org/10.1016/j.compositesb.2017.03.020

Shenoy, V.B., 2005. Atomistic calculations of elastic properties of metallic fcc crystal surfaces. Phys. Rev. B - Condens. Matter Mater. Phys. 71, 1–11. https://doi.org/10.1103/PhysRevB.71.094104

Shingare, K.B., Kundalwal, S.I., 2020. Flexoelectric and surface effects on the electromechanical behavior of graphene-based nanobeams. Appl. Math. Model. 81, 70–91. https://doi.org/10.1016/j.apm.2019.12.021

Shingare, K.B., Kundalwal, S.I., 2019. Static and dynamic response of graphene nanocomposite plates with flexoelectric effect. Mech. Mater. 134, 69–84. https://doi.org/10.1016/j.mechmat.2019.04.006

Shingare, K.B., Naskar, S., 2021a. Probing the prediction of effective properties for composite materials. Eur. J. Mech. A/Solids 87. https://doi.org/10.1016/j.euromechsol.2021.104228

Shingare, K.B., Naskar, S., 2021b. Effect of size-dependent properties on electromechanical behavior of composite structures, in: UK Association for Computational Mechanics (UK ACM 2021). pp. 0–4. https://doi.org/https://doi.org/10.17028/rd.lboro.14595696.v1

Shingare, Kishor Balasaheb, Naskar, S., 2021c. Analytical solution for static and dynamic analysis of graphene-based hybrid flexoelectric nanostructures. J. Compos. Sci. 5. https://doi.org/10.3390/jcs5030074

Shu, L., Li, F., Huang, W., Wei, X., Yao, X., Jiang, X., 2014. Relationship between direct and converse flexoelectric coefficients. J. Appl. Phys. 116. https://doi.org/10.1063/1.4897647

Shu, L., Liang, R., Rao, Z., Fei, L., Ke, S., Wang, Y., 2019. Flexoelectric materials and their related applications: A focused review. J. Adv. Ceram. https://doi.org/10.1007/s40145-018-0311-3

Shu, L., Wei, X., Pang, T., Yao, X., Wang, C., 2011. Symmetry of flexoelectric coefficients in crystalline medium, in: Journal of Applied Physics. https://doi.org/10.1063/1.3662196

Singh, A., Mukhopadhyay, T., Adhikari, S., Bhattacharya, B., 2021. Voltage-dependent modulation of elastic moduli in lattice metamaterials: Emergence of a programmable state-transition capability. Int. J. Solids Struct. 208–209, 31–48. https://doi.org/10.1016/j.ijsolstr.2020.10.009

Singhatanadgid, P., Singhanart, T., 2019. The Kantorovich method applied to bending, buckling, vibration, and 3D stress analyses of plates: A literature review. Mech. Adv. Mater. Struct. 26, 170–188. https://doi.org/10.1080/15376494.2017.1365984

Song, J., Zhou, J., Wang, Z.L., 2006. Piezoelectric and semiconducting coupled power generating process of a single ZnO belt/wire. A technology for harvesting electricity from the environment. Nano Lett. 6, 1656–1662. https://doi.org/10.1021/nl060820v

Song, M., Kitipornchai, S., Yang, J., 2017. Free and forced vibrations of functionally graded polymer composite plates reinforced with graphene nanoplatelets. Compos. Struct. 159, 579–588. https://doi.org/10.1016/j.compstruct.2016.09.070

Song, M., Yang, J., Kitipornchai, S., 2018. Bending and buckling analyses of functionally graded polymer composite plates reinforced with graphene nanoplatelets. Compos. Part B Eng. 134, 106–113. https://doi.org/10.1016/j.compositesb.2017.09.043

Sugino, C., Ruzzene, M., Erturk, A., 2018. Merging mechanical and electromechanical bandgaps in locally resonant metamaterials and metastructures. J. Mech. Phys. Solids 116, 323–333. https://doi.org/10.1016/j.jmps.2018.04.005

Talha, M., Singh, B.N., 2010. Static response and free vibration analysis of FGM plates using higher order shear deformation theory. Appl. Math. Model. 34, 3991–4011. https://doi.org/10.1016/j.apm.2010.03.034

Thomas, B., Roy, T., 2017. Vibration and damping analysis of functionally graded carbon nanotubes reinforced hybrid composite shell structures. JVC/Journal Vib. Control 23, 1711–1738. https://doi.org/10.1177/1077546315599680

Trindade, M.A., Benjeddou, A., 2009. Effective electromechanical coupling coefficients of piezoelectric adaptive structures: Critical evaluation and optimization. Mech. Adv. Mater. Struct. 16, 210–223. https://doi.org/10.1080/15376490902746863

Trinh, M.C., Mukhopadhyay, T., Kim, S.E., 2020. A semi-analytical stochastic buckling quantification of porous functionally graded plates. Aerosp. Sci. Technol. 105, 105928. https://doi.org/10.1016/j.ast.2020.105928

Vaishali, Mukhopadhyay, T., Karsh, P.K., Basu, B., Dey, S., 2020. Machine learning based stochastic dynamic analysis of functionally graded shells. Compos. Struct. 237, 111870. https://doi.org/10.1016/j.compstruct.2020.111870

Vatanabe, S.L., Rubio, W.M., Silva, E.C.N., 2014. Modeling of Functionally Graded Materials, in: Comprehensive Materials Processing. Elsevier, pp. 261–282. https://doi.org/10.1016/B978-0-08-096532-1.00222-3

Vidal, P., Polit, O., 2008. A family of sinus finite elements for the analysis of rectangular laminated beams. Compos. Struct. 84, 56–72. https://doi.org/10.1016/j.compstruct.2007.06.009

Wang, B., Li, X.F., 2021. Flexoelectric effects on the natural frequencies for free vibration of piezoelectric nanoplates. J. Appl. Phys. 129. https://doi.org/10.1063/5.0032343

Wang, L., Hu, H., 2005. Flexural wave propagation in single-walled carbon nanotubes. Phys. Rev. B - Condens. Matter Mater. Phys. 71. https://doi.org/10.1103/PhysRevB.71.195412

Wang, X., Zhou, J., Song, J., Liu, J., Xu, N., Wang, Z.L., 2006. Piezoelectric field effect transistor and nanoforce sensor based on a single ZnO nanowire. Nano Lett. 6, 2768–2772. https://doi.org/10.1021/nl061802g

Wang, X., Zhou, K., 2013. Twelve-dimensional Stroh-like formalism for Kirchhoff anisotropic piezoelectric thin plates. Int. J. Eng. Sci. 71, 111–136. https://doi.org/10.1016/j.ijengsci.2013.06.004

Wang, Y., Xie, K., Fu, T., 2020. Vibration analysis of functionally graded graphene oxide-reinforced composite beams using a new Ritz-solution shape function. J. Brazilian Soc. Mech. Sci. Eng. 42. https://doi.org/10.1007/s40430-020-2258-x

Xu, K., Wang, K., Zhao, W., Bao, W., Liu, E., Ren, Y., Wang, M., Fu, Y., Zeng, J., Li, Z., Zhou, W., Song, F., Wang, X., Shi, Y., Wan, X., Fuhrer, M.S., Wang, B., Qiao, Z., Miao, F., Xing, D., 2015. The positive piezoconductive effect in graphene. Nat. Commun. 6. https://doi.org/10.1038/ncomms9119

Yan, Zhi, Jiang, L., 2012. Surface effects on the electroelastic responses of a thin piezoelectric plate with nanoscale thickness. J. Phys. D. Appl. Phys. 45. https://doi.org/10.1088/0022-3727/45/25/255401

Yan, Z., Jiang, L.Y., 2012. Vibration and buckling analysis of a piezoelectric nanoplate considering surface effects and in-plane constraints. Proc. R. Soc. A Math. Phys. Eng. Sci. 468, 3458–3475. https://doi.org/10.1098/rspa.2012.0214

Yang, B., Kitipornchai, S., Yang, Y.F., Yang, J., 2017. 3D thermo-mechanical bending solution of functionally graded graphene reinforced circular and annular plates. Appl. Math. Model. 49, 69–86. https://doi.org/10.1016/j.apm.2017.04.044

Yang, F., Chong, A.C.M., Lam, D.C.C., Tong, P., 2002. Couple stress based strain gradient theory for elasticity. Int. J. Solids Struct. 39, 2731–2743. https://doi.org/10.1016/S0020-7683(02)00152-X

Yang, J., Chen, D., Kitipornchai, S., 2018. Buckling and free vibration analyses of functionally graded graphene reinforced porous nanocomposite plates based on Chebyshev-Ritz method. Compos. Struct. 193, 281–294. https://doi.org/10.1016/j.compstruct.2018.03.090

Yang, W., Liang, X., Shen, S., 2015. Electromechanical responses of piezoelectric nanoplates with flexoelectricity. Acta Mech. 226, 3097–3110. https://doi.org/10.1007/s00707-015-1373-8

Zhang, Chunli, Chen, W., Zhang, Ch, 2013. Two-dimensional theory of piezoelectric plates considering surface effect. Eur. J. Mech. A/Solids 41, 50–57. https://doi.org/10.1016/j.euromechsol.2013.02.005

Zhang, J., Wang, C., Adhikari, S., 2012. Surface effect on the buckling of piezoelectric nanofilms. J. Phys. D. Appl. Phys. 45. https://doi.org/10.1088/0022-3727/45/28/285301

Zhang, Z., Yan, Z., Jiang, L., 2014. Flexoelectric effect on the electroelastic responses and vibrational behaviors of a piezoelectric nanoplate. J. Appl. Phys. 116. https://doi.org/10.1063/1.4886315

Zhao, S., Zhao, Z., Yang, Z., Ke, L.L., Kitipornchai, S., Yang, J., 2020. Functionally graded graphene reinforced composite structures: A review. Eng. Struct. https://doi.org/10.1016/j.engstruct.2020.110339

Zhao, Z., Ni, Y., Zhu, S., Tong, Z., Zhang, J., Zhou, Z., Lim, C.W., Xu, X., 2020. Thermo-Electro-Mechanical Size-Dependent Buckling Response for Functionally Graded Graphene Platelet Reinforced Piezoelectric Cylindrical Nanoshells. Int. J. Struct. Stab. Dyn. 20. https://doi.org/10.1142/S021945542050100X

Zhou, Y., Liu, J., Hu, X., Chu, B., Chen, S., Salem, D., 2017. Flexoelectric effect in PVDF-based polymers. IEEE Trans. Dielectr. Electr. Insul. 24, 727–731. https://doi.org/10.1109/TDEI.2017.006273